Nanostructured ceria-based catalysts doped with La and Nd: How acid-base sites and redox properties determine the oxidation mechanisms

Nanostructured ceria-based catalysts doped with La and Nd: how acid-base sites and redox properties determine the oxidation mechanisms

Enrico Sartoretti[a], Chiara Novara[a], Angelica Chiodoni[b], Fabrizio Giorgis[a], Marco Piumetti[a]*, Samir Bensaid[a], Nunzio Russo[a], Debora Fino[a]

[a] Department of Applied Science and Technology, Politecnico di Torino, Corso Duca degli Abruzzi, 24, 10129 Torino, Italy.

[b] Center for Sustainable Future Technologies @Polito, Istituto Italiano di Tecnologia, Via Livorno 60, 10144 Torino, Italy

* Corresponding author:

E-mail address: marco.piumetti@polito.it (Marco Piumetti)

Catalysis Today https://doi.org/10.1016/j.cattod.2021.11.040

Keywords: Mixed oxides, Ceria, Lanthanum, Neodymium, Praseodymium, Soot oxidation

ABSTRACT

In the present work, novel ceria-based nanocatalysts containing different quantities of La and Nd were prepared via hydrothermal synthesis. The effects of doping on the structural and physico-chemical properties of ceria were examined with several techniques, such as XRD, FESEM, TEM, Raman spectroscopy, XPS, H_2-TPR and O_2/NH_3/CO_2-TPD. The catalytic activity of doped ceria towards CO, NO and soot oxidation was evaluated in different conditions; in particular, the role of the catalyst-soot contact and the influence of NO_x and water on the soot oxidation performances were investigated. La and Nd ions were well incorporated in ceria structure, but the final morphology was significantly altered. The introduction of trivalent cations was also associated with a higher abundance of defects and oxygen vacancies, but an excessive oxygen deficiency detrimentally affected the material reducibility and catalytic activity for CO and NO oxidation. Conversely, soot oxidation benefited from La and Nd addition. In particular, the Ce-La equimolar oxide exhibited outstanding performances in all the tested conditions, thanks to its optimal morphology and surface acidity. A detailed comparison with equimolar ceria-praseodymia allowed to investigate how acid-base sites and redox properties control the different catalytic mechanisms involved in standard and NO_x-assisted soot oxidation.

1. Introduction

In the last years, several nations have issued strict regulations in order to further limit the polluting emissions of all types of vehicles [1]. New CO_2 emission targets have also been introduced, with the purpose of fighting against global warming (e.g., 95 g km^{-1} for passenger cars by 2021in the European Union) [2]. Diesel engines, characterized by high efficiency and low fuel consumption, represent a crucial technology in order to comply with these targets, especially in the case of light duty and heavy duty vehicles. However, they also present some well-known drawbacks, such as the production of significant quantities of particulate matter (PM) or nitrogen oxides (NO_x), which are harmful to human health [3]. For this reason, Diesel vehicles are today equipped with a complex aftertreatment apparatus able to keep the emissions within the limits [1,4].

Concerning PM, it can be effectively abated by Diesel particulate filters, i.e. wall-flow monoliths with porous walls able to entrap fine dusts with a high efficiency. However, these filters must be periodically regenerated by increasing the temperature so as to cause the combustion of carbon particles (also known as soot) [5]. In order to lower the fuel consumption associated with the regeneration step, as well as the temperature and time required, proper catalysts can be deposited on the filter walls with the aim of favoring soot oxidation [6,7]. In particular, ceria-based materials have been widely studied for this application in the last decades, as alternatives to the highly expensive noble metals [8–10].

Ceria possesses excellent redox properties and high oxygen storage capacity, due to the ability of cerium to easily shift its oxidation state from Ce^{4+} to Ce^{3+}. Furthermore, different types of nanostructured ceria particles can be prepared by tuning the synthesis procedure [11]. A well-defined morphology can bring significant benefits, since ceria reactivity depends on the exposed crystal facets [12–14]. Moreover, the size and shape of the nanoparticles also affect the quality and the number of catalyst-soot contact points, which are crucial aspects in the case of soot oxidation [15,16].

Three main soot oxidation pathways have been identified in the case of ceria-based materials. In detail, a Mars–van Krevelen-like mechanism (MvK) can occur at the catalyst-soot interface, involving direct oxidation of soot by lattice oxygen coming from the catalyst; the thus-created oxygen vacancies are then refilled by gaseous O_2 [12,13]. Besides, reactive oxygen species such as O_2^- or O^- ions forming at the catalyst surface can be delivered to soot particles through spillover [17,18]. Furthermore, the NO_x present in Diesel exhausts can also take part in the reactions, by adsorbing at the catalyst surface or by directly oxidizing soot [19–22].

The physico-chemical and structural properties governing the catalytic activity of ceria-based materials can be further improved by doping [22]. In fact, the insertion of dopant ions into ceria lattice can foster the creation of defects and oxygen vacancies, which are directly involved in the catalysis [23–25]. Among the possible dopants, rare earth elements are of interest since they can be easily incorporated in ceria lattice. In particular, excellent performances for soot oxidation have been recently obtained with Pr-doped ceria [22,26], especially in the case of nanostructured equimolar mixtures [21,27]. La and Nd also proved to be interesting dopants for ceria-based materials: indeed, these elements can improve ceria redox properties and are able to foster the generation and the effective transfer of highly reactive oxygen species, boosting soot oxidation [28–31]. However, to the best of authors' knowledge, the catalytic properties of well-defined ceria-based nanoparticles with a high loading of La and Nd have not yet been investigated.

In the present work, six ceria-based oxides containing different quantities of La or Nd (10, 25 or 50%) were prepared via hydrothermal synthesis and evaluated as oxidizing catalysts. These mixed materials were deeply investigated with various characterization techniques and compared with pure oxides, in order to study the effects of doping on the structure, morphology, defectiveness, surface acidity and chemical/redox properties. The influence of these features on the catalytic activity towards soot oxidation was discussed, also taking into account the CO and NO oxidation capability. In detail, soot oxidation tests were carried out in different conditions, probing two degrees of contact between the catalyst and soot and evaluating the catalyst stability upon thermal aging and in the presence of water. Finally, NO_x-assisted soot oxidation was investigated, assessing the catalytic performances and suggesting the reaction mechanisms involved.

2. Experimental

2.1 Catalyst synthesis

The six materials investigated in this study were prepared by doping ceria with different quantities (i.e. 10%, 25% or 50% atomic) of lanthanum or neodymium. The samples were named CeXXReYY, where Re is the doping rare earth (La or Nd) while XX and YY are the atomic percentages of Ce and of the doping element, respectively. A hydrothermal synthesis route was used, following a procedure reported elsewhere [23,32]. In brief, 48 g of NaOH (Carlo Erba Reagents) were dissolved in 70 mL of deionized water, stirring for 30 min to dissipate the released heat. Meanwhile, another solution was prepared by mixing appropriate amounts (20 mmol in all) of $Ce(NO_3)_3 \cdot 6H_2O$, $La(NO_3)_3 \cdot 6H_2O$ or $Nd(NO_3)_3 \cdot 6H_2O$ (all provided by Sigma-Aldrich) in 10 mL of deionized water. The latter solution was then slowly added dropwise to the first one, stirring for 1 h at room temperature (RT). The thus obtained cloudy mixture was then poured into a PTFE liner and placed into a stainless steel autoclave, which was put in an oven and heated at 180 °C for 24 h. Afterwards, the muddy precipitate was rinsed several times with deionized water and ethanol and dried at 70 °C overnight. Finally, the powder obtained was gently ground in a mortar and calcined in an oven at 650 °C for 4 h.

For the sake of comparison, pure CeO_2, La_2O_3 and Nd_2O_3, as well as equimolar ceria-praseodymia (Ce50Pr50), were also synthesized, following an analogous procedure.

2.2 Catalyst characterization

A Philips X'Pert PW3040 diffractometer was employed to perform X-ray diffraction (XRD), using Cu Kα radiation (λ = 1.5418×10^{-10} m), a 0.013° step size and a 0.2 s/step acquisition time. The assignation of the diffraction peaks was carried out referring to the Powder Diffraction Files database (International Centre of Diffraction Data). Scherrer's equation was used for calculating the average crystallite size, correcting the instrumental peak broadening with a LaB_6 calibration standard. The Nelson-Riley extrapolation function was employed to estimate the lattice parameters.

The surface area and pore-related properties of the prepared catalysts were investigated via nitrogen physisorption, which was performed in a Micromeritics Tristar II 3020 after pre-treating the powder at 200 °C for 2 h under nitrogen flow. The specific surface area was estimated using the Brunauer–Emmett–Teller (BET) method, while the pore volume and pore average size were evaluated applying the Barrett-Joyner-Halenda (BJH) algorithm to the desorption branch.

Field emission scanning electron microscopy (FESEM) was performed in a Zeiss Merlin with a Gemini-II column and an Oxford x-act X-ray detector. Prior to the morphological analysis, the powder was coated with a 5 nm thick layer of platinum via sputter deposition. The chemical composition of the samples was estimated via energy-dispersive X-ray spectroscopy (EDX), performed on non-coated powder.

Transmission electron microscopy (TEM) was performed with a FEI Tecnai F20ST operating at 200 kV. High angle annular dark field (HAADF) and energy dispersive X-ray spectroscopy (EDX, EDAX) detectors were used in scanning TEM (STEM) mode. The samples were prepared by suspending the powder in ethanol. A suspension droplet was then deposited on a standard holey carbon TEM Cu grid, analyzing the specimen after the complete evaporation of the solvent

Room temperature Raman spectra were recorded at 514.5 nm in backscattering configuration using a 5x objective of a Renishaw InVia Reflex Raman microscope. Three spectra were acquired at different locations of each sample with an exposure time of 225 s and a laser excitation power of 10 mW. The areas of the whole defect-induced band (D band, located between 500 and 650 cm^{-1}) and the main F_{2g} peak (located between 400 cm^{-1} and 500 cm^{-1}) were determined by spectral deconvolution to calculate the D/F_{2g} ratio, which is indicative of the defect density of the catalysts. In detail, six curves were needed to fit the 200 – 750 cm^{-1} range, as proposed in [33], with two Lorentzian profiles used for the deconvolution of both the D and F_{2g} bands. In situ Raman measurements were carried out during soot oxidation, using a Linkam TS1500 cell. Appropriate quantities of catalyst and Printex-U soot (weight ratio 40:1) were mixed in a ball mill and then compressed to obtain a small tablet, which was placed in the cell and heated in air flow (45 mL min^{-1}) using a 3 °C min^{-1} ramp up to 700 °C.

A PHI Versa Probe instrument was employed to perform X-ray photoelectron spectroscopy (XPS) on catalyst powder (187.85 eV band-pass energy, 45° take-off angle, 100.0 μm X-ray spot size). The XP spectra were referenced to the C 1s core level at 284.8 eV, in order to compensate the surface charging effect. Casa XPS software was used for data analysis.

H_2 temperature programmed reduction (TPR) analyses was carried out in a Thermo Scientific 1100 TPDRO. Some catalyst powder (50 mg) was placed in a quartz reactor, between two quartz wool layers. An oxidative pre-treatment was carried out by heating the sample up to 550 °C with a 10 °C/min ramp in O_2 flow, maintaining this temperature for 50 min and then flushing the reactor with N_2 during cooling. The sample was then heated from 50 up to 900 °C with a 10 °C min^{-1} ramp, while flowing 20 mL min^{-1} of 5% H_2 in Ar.

The same instrument was employed to carry out O_2 temperature programmed desorption (TPD), using 100 mg of powder. The samples were pretreated in oxygen at 550 °C for 30 min, keeping the oxygen flow during the successive cooling. The desorption was performed by heating the reactor from RT up to 950 °C with a 5 °C min^{-1} ramp under a 20 mL min^{-1} flow of He.

NH_3-TPD was performed using the same equipment: 100 mg of catalyst were pretreated at 550 °C for 2 h in He flow, then the acid sites at the surface were saturated by flowing 20 mL min^{-1} of a mixture containing 10% NH_3 in He at 100 °C for 30 min; after flushing away physisorbed ammonia by flowing pure He for 30 min at 120 °C, desorption was carried out by heating the reactor up to 600 °C with a 10 °C min^{-1} ramp under a 20 mL min^{-1} flow of He.

CO_2-TPD was carried out analogously: 100 mg of catalyst were pretreated at 550 °C for 2 h in He flow, then the basic sites at the surface were saturated by flowing 30 mL min^{-1} of pure CO_2 at RT for 30 min; after flushing away physisorbed CO_2 by flowing pure He for 30 min at 50 °C, desorption was carried out by heating the reactor up to 600 °C with a 10 °C min^{-1} ramp under a 20 mL min^{-1} flow of He.

2.3. Catalytic activity

The temperature-programmed oxidation (TPO) tests were performed in a PID-controlled furnace, using a quartz U-tube reactor containing the catalytic bed and a K-type thermocouple, whose tip was placed closed to the catalytic bed. A by-pass line allowed to stabilize the feed gas concentration before starting the tests. An ABB AO2020 NDIR gas analyzer was used to monitor the concentration of CO and CO_2 in the reactor outlet, while the concentration of NO, NO_2 and O_2 was measured with an Emerson XStream NDIR/paramagnetic gas analyzer. Using this general setup, different types of catalytic tests were performed.

2.3.1. CO oxidation

CO oxidation was carried out using 100 mg of catalyst. The bed was pre-treated at 100 °C for 30 min under a 50 mL min^{-1} flow of air. The reactor was then cooled to 50 °C, while a 50 mL min^{-1} flow of a mixture containing 1000 ppm of CO and 10% of O_2 in N_2 was sent to the by-pass line. After the concentration of CO, CO_2 and O_2 had stabilized, the flow was sent to the reactor. After reaching the steady state, the gas composition at the outlet was recorded and then the oven temperature was increased by 50 °C. This procedure was repeated different times, sampling a sequence of steady states until total CO conversion. The specific reaction rate of CO oxidation (r_{CO}) was calculated using equation (1), where $C_{CO,in}$ and $C_{CO,out}$ are the concentrations of CO in the reactor inlet and outlet, respectively, F is the gas molar flow rate, m is the sample mass and SSA is the specific surface area of the catalyst.

(1) $$r_{CO} = \frac{(C_{CO,in} - C_{CO,out}) \cdot F}{m \cdot SSA}$$

2.3.2. NO oxidation

In this test, the catalytic bed was prepared by mixing with a spatula 45 mg of catalyst and 150 mg of SiO_2 (Sigma-Aldrich). The bed was pre-treated in air (100 mL min^{-1}) for 30 min at 100 °C, then it was cooled to 50 °C. A gas mixture with 10% of O_2 and 550 ppm of NO in N_2 (100 mL min^{-1}) was sent to the by-pass line in the meantime, and this flow was sent to the reactor when the concentrations of NO, NO_2 and O_2 were stable. Once a steady state was reached, the oven temperature was increased by 50 °C after recording the outlet gas composition. This procedure was repeated several times, sampling a sequence of steady states between 50 and 650 °C.

2.3.3. Soot oxidation

A catalytic bed with 45 mg of catalyst, 5 mg of Printex-U soot (Degussa) and 150 mg of SiO_2 (Sigma-Aldrich) was prepared and used during soot oxidation tests. Two different degrees of contact were examined: *tight contact* (TC) conditions were achieved by milling together the different powders in a ball mill (15 min at 290 rpm), while *loose contact* (LC) conditions were achieved by gently mixing the powders for few minutes using a spatula. The catalytic bed was then inserted in the reactor and pre-treated in air (100 mL min^{-1}) for 30 min at 100 °C. During the test, a mixture with 10% of O_2 in N_2 (100 mL min^{-1}) was sent to the reactor and the oven temperature was raised from 100 up to 700 °C with a 5 °C min^{-1} ramp.

In order to evaluate the catalyst stability, soot oxidation was repeated after aging the samples at 700 °C for 8 h in an oven. The effect of water was instead assessed by performing soot oxidation tests in loose contact feeding the reactor with a mixture of 10% of O_2 and 10% of H_2O in N_2, prepared using a Bronkhorst CEM evaporator.

NO_x-assisted soot oxidation tests were also performed. In this case, the catalytic bed was prepared and pre-treated as described above. Successively, a gas mixture with 10% of O_2 and 550 ppm of NO in N_2 was sent to the by-pass line and then to the reactor. After the gas analyzer signals had stabilized, the temperature was increased from 50 up to 700 °C with a 5 °C min^{-1} ramp.

For the sake of comparison, uncatalyzed soot oxidation was also performed with the same procedures, but preparing the bed by mixing 195 mg of SiO_2 and 5 mg of Printex-U soot.

3. Results and Discussion

3.1. Catalyst characterization

3.1.1. Structural and textural properties

The powder XRD diffractograms of the six materials are reported in Fig. 1, together with those of pure CeO_2, La_2O_3 and Nd_2O_3. Pure ceria exhibits a pattern with eight peaks, typical of fluorite crystal structure [27,34–36]. Doped ceria is characterized by analogous diffractograms, but with some differences that become more evident increasing the dopant loading. In fact, the XRD patterns of the doped samples present a progressive shift towards lower angles with respect to that of pure ceria, as displayed in the insets of Fig. 1. Moreover, only Ce90Nd10 is characterized by symmetric peaks, while all the other catalysts show a shoulder on the left side of each reflection, or even two distinct sets of peaks in the case of the Ce50La50 and Ce50Nd50 equimolar mixtures.

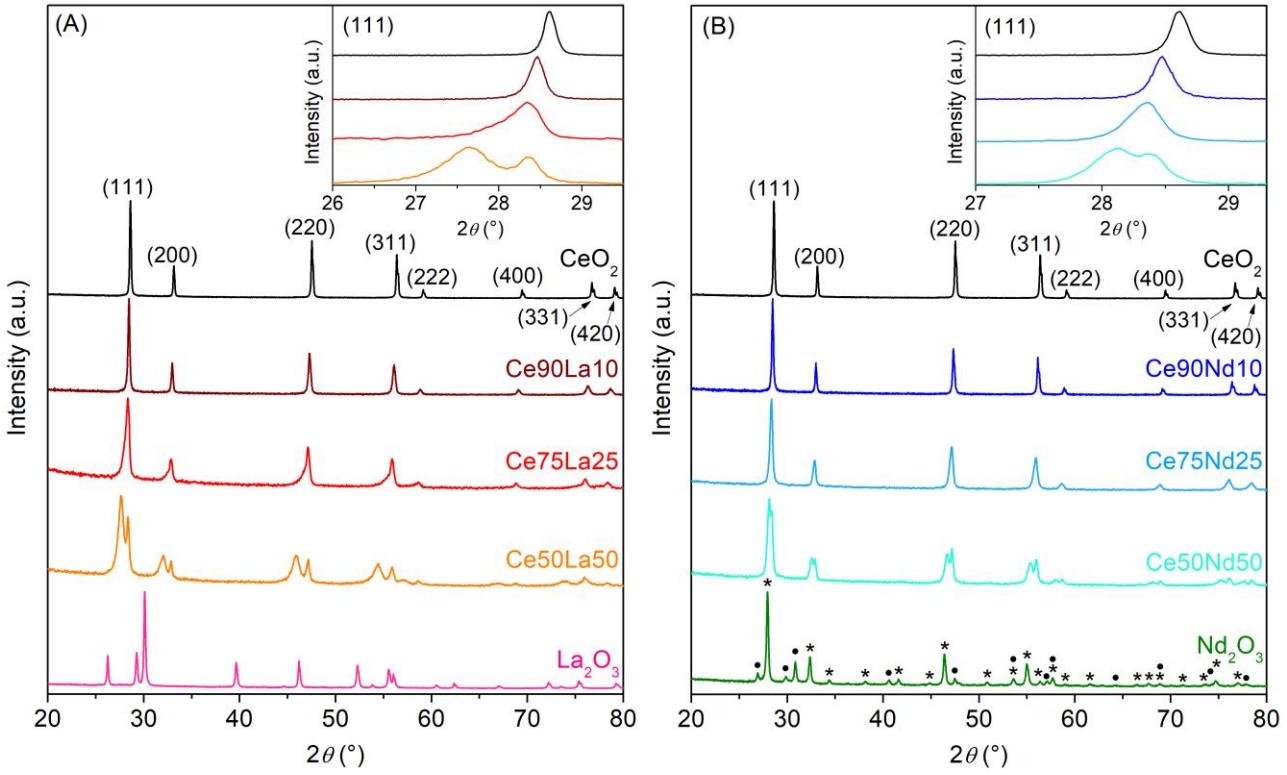

Fig. 1. XRD diffractograms of the La-doped (A) and Nd-doped (B) ceria-based catalysts. As a comparison, the patterns of the pure oxides (CeO_2, La_2O_3 and Nd_2O_3, prepared following the same synthesis procedure) are also reported. For the biphasic Nd_2O_3, the peaks of the cubic (✳) and hexagonal (●) crystal structures are distinguished. In the insets, the (111) peak of the fluorite lattice is magnified.

However, this behavior does not seem related to La or Nd segregation. In fact, the typical peaks of the La_2O_3 hexagonal structure [37,38] are completely absent in the patterns of La-doped ceria, as evident from Fig. 1 A, suggesting that La ions are somehow incorporated in the ceria lattice at high La loading too. The situation is similar for Nd-doped ceria, although this time the presence of small crystals of segregated Nd_2O_3 cannot be completely ruled out: indeed,

neodymium oxide can form two different phases, with cubic and hexagonal structures [39,40], and the main peaks of the former crystal unit are partially overlapped to those of ceria, as displayed in Fig. 1 B.

Nevertheless, the presence of ceria-based particles with different compositions can be expected in the doped catalyst powder. The appearance of two sets of XRD peaks might therefore signal a bimodal distribution of the crystals [41], pointing out the existence of two main phases in the mixed oxides with two slightly different cubic structures. The first phase, characterized by higher-angle peaks, could be richer in cerium, since it has a smaller elementary unit and is more abundant in the slightly doped samples. The other phase, giving rise to lower-angle peaks, could present a more reduced structure rich in big trivalent cations, since it has a larger crystal unit and becomes dominant as the dopant loading is increased.

For all the catalysts, the lattice constant (a) and the average crystallite size (D_c) of each detected phase were calculated and the values are reported in Table 1. The variation of the lattice constant as a function of doping is also detailed in Fig. 2. The unit cell size of the dopant-enriched reduced structures increases almost linearly with the dopant content. The unit cell of the cerium-enriched oxidized structures undergoes an enlargement at increasing dopant loading too, but a plateau is reached in this case. Lattice expansion, which is especially remarkable in the case of La doping, is the result of the insertion of La^{3+} and Nd^{3+} ions in ceria structure: indeed, the ionic radii of these species (1.16 and 1.109 Å, respectively) are larger than that of the Ce^{4+} ions they replace (0.97 Å) [42]. A higher abundance of Ce^{3+} in doped ceria could contribute to this effect as well. The progressive expansion of the crystal unit cells can explain the gradual shift observed in the XRD patterns of the doped samples (insets of Fig. 1) [43]. Concerning the average crystallite size, it is always higher for the identified Ce-rich phase (right peaks); moreover, it becomes lower for both the phases as the dopant loading increases: this means that doping affects the particle growth during the synthesis, hindering the formation of big crystals [44].

Table 1

Structural properties of the catalysts.

Catalyst	**XRD peaks considered** [a]	**a** [a] (nm)	**D_C** [a] (nm)	**SSA** [b] ($m^2\ g^{-1}$)	**V_p** [b] ($cm^3\ g^{-1}$)	**D_p** [b] (nm)	**D/F_{2g}** [c]
CeO_2	Sole set of peaks (2Θ = 28.59, 33.12, 47.52, 56.38, 59.13, 69.44, 6.73, 79.10°)	0.5412	144	7	0.054	30	0.03
Ce90La10	Set of left peaks (2Θ = 28.35, 32.88, 47.10, 55.92, 58.70, 68.91, 76.08, 78.50°)	0.5447	42	9	0.037	16	0.16
	Set of right peaks (2Θ = 28.45, 32.96, 47.27, 56.07, 58.81, 69.07, 76.30, 78.64°)	0.5438	103				
Ce75La25	Set of left peaks (2Θ = 28.02, 32.40, 46.70, 55.40, 58.18, 67.90, 75.40, 77.35°)	0.5495	12	14	0.041	12	0.31
	Set of right peaks (2Θ = 28.34, 32.82, 47.10, 55.87, 58.64, 68.80, 76.00, 78.31°)	0.5455	38				
Ce50La50	Set of left peaks (2Θ = 27.61, 31.96, 45.84, 54.34, 57.05, 66.89, 73.77, 76.03°)	0.5592	11	18	0.047	10	0.97
	Set of right peaks (2Θ = 28.34, 32.82, 47.09, 55.85, 58.62, 68.77, 75.95, 78.28°)	0.5458	36				
Ce90Nd10	Sole set of peaks (2Θ = 28.45, 32.97, 47.32, 56.13, 58.87, 69.14, 76.39, 78.75°)	0.5431	109	10	0.075	27	0.18

Ce75Nd25	Set of left peaks (2Θ = 28.21, 32.71, 46.99, 55.73, 58.00, 68.70, 75.85, 78.20°)	0.5466	36	13	0.066	20	0.45
	Set of right peaks (2Θ = 28.35, 32.85, 47.17, 55.94, 58.60, 68.90, 76.11, 78.46°)	0.5447	66				
Ce50Nd50	Set of left peaks (2Θ = 28.09, 32.52, 46.64, 55.31, 57.99, 68.08, 75.19, 77.53°)	0.5506	20	12	0.038	12	1.44
	Set of right peaks (2Θ = 28.40, 32.89, 47.17, 55.95, 58.67, 68.91, 76.07, 78.42°)	0.5451	58				

[a] Lattice constant (a) and average crystallite size (D_C) estimated via XRD considering the specified peaks (for D_C estimation only the first four peaks were used, since the other ones are characterized by too low intensity)
[b] Specific surface area (SSA), total pore volume (V_p) and average pore diameter (D_p) obtained via N_2-physisorption
[c] D/F_{2g} ratio calculated through Raman spectra deconvolution

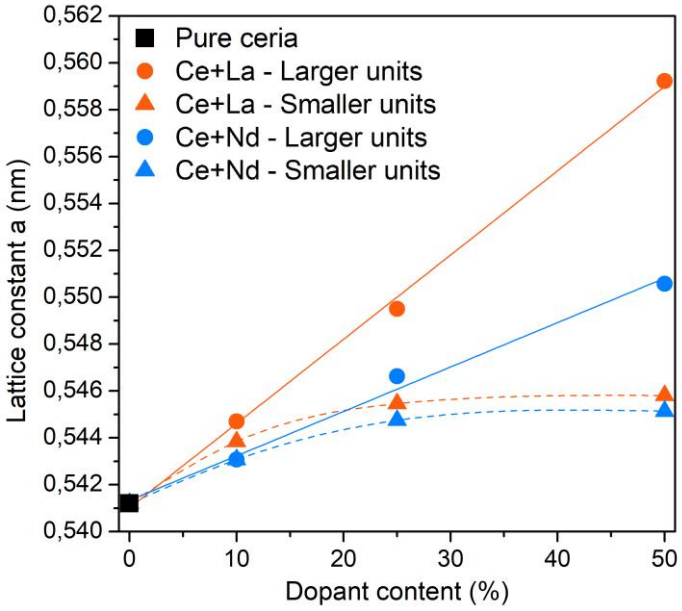

Fig. 2. Variation of the lattice constant (a) as a function of doping for the two different types of crystal units identified in ceria doped with La and Nd.

La and Nd doping influenced the specific surface area of the catalysts too, as shown by the values in Table 1. In fact, the dopant addition caused an increase in surface area, which is in agreement with the smaller size of the crystallites previously discussed. This effect is more marked for the Ce-La mixed oxides, which are indeed characterized by lower D_c values. As a result, the Ce75La25 and Ce50La50 samples exhibit the highest specific surface area. The pore volume of the six samples changes too, but with different trends: this parameter increases with La addition, while it decreases when Nd is incorporated in ceria. However, all the catalysts present a quite low pore volume, limited to that of the interparticle voids, as expected for non-porous powders. The doping also causes a drop in the average pore diameter, especially in the Ce-La mixed oxides, which is likely the result of the smaller particle size.

The morphology of the catalysts was investigated via electron microscopy. As previously described in the literature [11,45], the synthesis route employed here allows to obtain pure ceria in the form of well-defined cubic nanoparticles, with size ranging from 50 to 400 nm (Fig. 3 G). However, the morphology changes upon doping, as shown by the FESEM micrographs of the mixed oxides displayed in Fig. 3 A-F. Actually, only Ce90Nd10 preserves a purely nanocubic structure similar to that of CeO_2, albeit characterized by smaller particles in the 50 – 300 nm range. The other five catalysts exhibit nanocubic shapes too, with reduced particle dimensions as the dopant concentration increases, but

rod-like structures can be noticed besides. The elongated particles become more abundant with increasing dopant loading and they even constitute the prevalent morphological species in the two equimolar oxides.

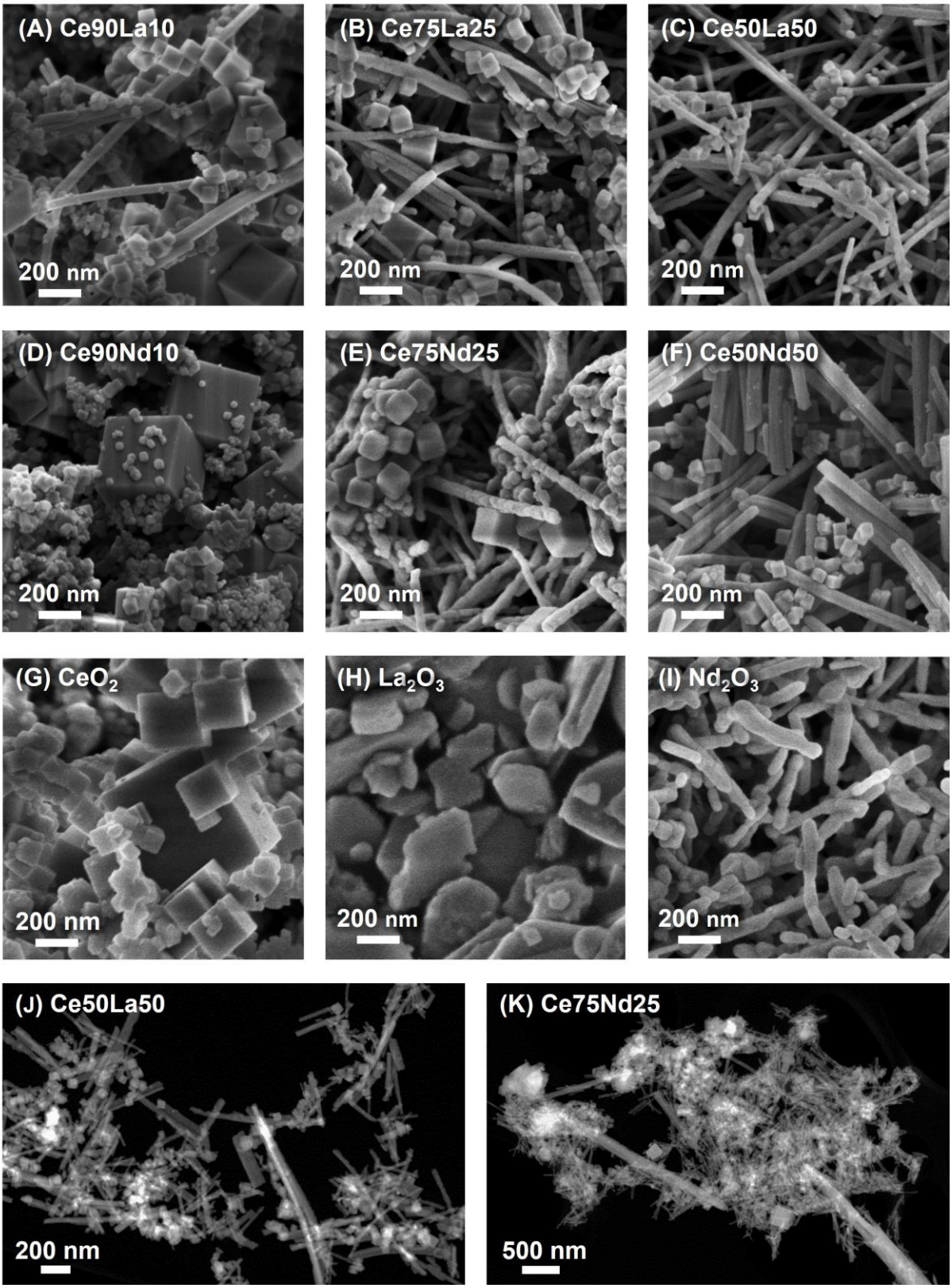

Fig. 3. FESEM micrographs of the Ce90La10 (A), Ce75La25 (B), Ce50La50 (C), Ce90Nd10 (D), Ce75Nd25 (E) and Ce50Nd50 (F) catalysts, compared with pure CeO_2 (G), La_2O_3 (H) and Nd_2O_3 (I). STEM images of the Ce50La50 (J) and Ce75Nd25 (K) samples.

The incorporation of La and Nd in ceria structure has therefore two main effects on the particle ripening process: the dopant ions hinder the crystal growth, fostering the formation of smaller nanocubes, and at the same time favor the elongation of the particles. Furthermore, the two crystalline phases detected by XRD could correspond to the two different shapes: the cubes likely consist of Ce-rich bigger crystals with smaller and less distorted unit cells, while the rods might contain a higher quantity of dopant ions and be formed by several small crystals with larger and more deformed unit cells. Anyway, the morphology of the mixed oxides is different from that of the La_2O_3 and Nd_2O_3 irregular particles (shown in Fig. 3 H and I, respectively), consistently with the absence of segregated pure oxides.

EDX analysis was performed focusing the spot on different points of the sample. The thus obtained average dopant concentration in the bulk of the mixed oxides is reported in Table 2 and all the values result to be very close to the nominal ones. Furthermore, an EDX map was collected on the Ce50La50 sample (shown in Fig. S1) and similar uniform signals were obtained for Ce and La. However, because of the limited resolution of this technique, an even distribution of the two elements can be assumed only at micrometric level. In order to further investigate the compositional differences between cubes and rods, a linear map was acquired on the same sample (results reported in Fig. S2). A line crossing a group of nanocubes amidst fibers was chosen and on the central agglomeration of cubic nanoparticles a more intense O signal and a lower La signal were recorded, while Ce signal only slightly increased compared to that of the surrounding region. Hence, these results support the attribution of a Ce-richer and more oxidized structure to the nanocubes.

In order to better assess the structural and compositional properties of the two best performing catalysts (i.e. Ce50La50 and Ce75Nd25, as shown later on), a transmission electron microscopy characterization was performed, both in TEM and in STEM mode. Regarding the Ce50La50 sample, the STEM image in Fig. 3 J confirms what found with FESEM. This catalyst contains cubic crystals, with a size of tens of nanometers, and different wired crystals, with variable length, from 100-200 nm to some microns, and diameters in the range of 20-100 nm. TEM analysis put in evidence that the cubes are almost single crystals (Fig. S3 A), while the wires frequently show a polycrystalline nature (Fig. S3 B). In addition, some round particles can also be found. All the crystals show a certain degree of local disorder, probably due to the La loading, more evident in the wired crystals. The X-ray spectroscopy microanalysis performed both in a group of crystals and on a single cube and a single wire shed some light about their composition. The semiquantitative analysis of the EDX spectrum of a big group of crystals show a relative Ce/La composition very close to the nominal one (Fig. S3 C). However, the spectra acquired on a single cube and a single wire, reported in Fig. S4, suggest that the cubes have a lower La content with respect to the wires, supporting the previously proposed hypothesis.

Also concerning the Ce75Nd25 catalyst, the STEM image in Fig. 3 K confirms the FESEM results. In this sample, cubes and wires with a more variable range of sizes and lengths can be found. The wires are fully polycrystalline, as very clear in the FESEM image in Fig. 3 E and also evident in TEM characterization (shown in Fig. S5 A and B). Nevertheless, the Ce75Nd25 crystals exhibit a lower degree of disorder, with respect to the Ce50La50 ones. The semiquantitative analysis of the EDX spectrum almost confirms the nominal dopant content (Fig. S5 C).

Raman spectroscopy was used to analyze the effects induced by doping on the microstructure and defectiveness of the catalysts. The Raman spectra of the ceria-based samples are reported in Fig. 4. The spectra are featured by an intense vibrational mode located at 465 cm^{-1} for pure ceria, that is ascribed to the symmetric stretching of the CeO_8 unit in the fluorite structure (F_{2g} mode); besides, a weaker band around 600 cm^{-1} arises in the presence of defects (D band) [23,46]. The addition of different amounts of dopants clearly affects both the main bands. In detail, the F_{2g} mode significantly shifts towards lower wavenumber, due to the expansion of the unit cell upon the incorporation of larger cations and to the generation of new defects. At the same time, the structure distortion accounts for an asymmetric broadening of the F_{2g} peak, as previously reported for rare earth-doped ceria [47]. All the described effects become more evident by increasing the dopant concentration. As expected, no splitting of the main band is detected despite the mixture consists of two different families of nanostructures (rods and cubes), as they retain the same crystalline phase. Nevertheless, the very broad linewidth of the F_{2g} peak at high dopant concentration is consistent with a heterogeneous distribution of dopants and defect sites in the two nanoshapes.

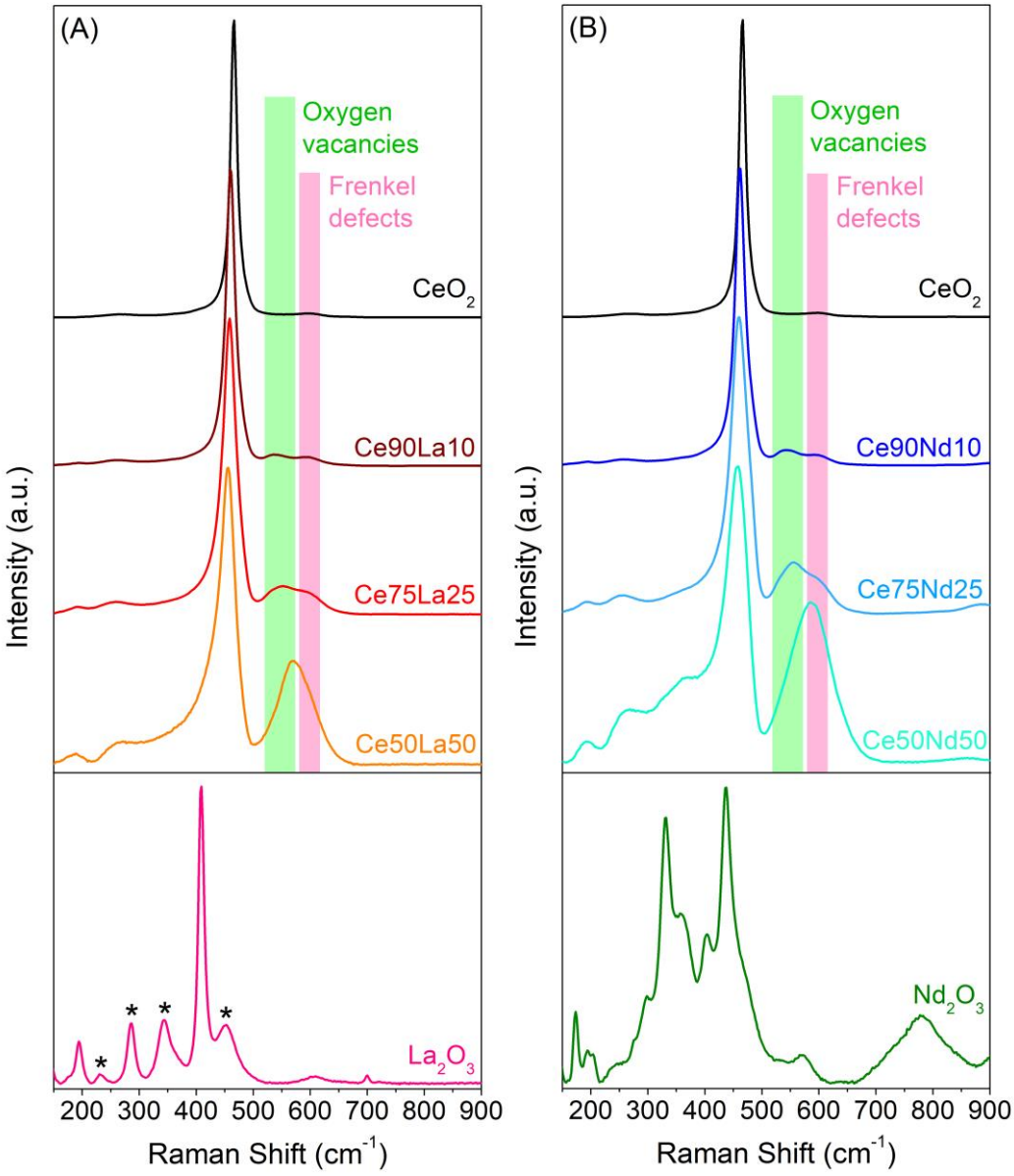

Fig. 4. Raman spectra collected at RT on the La-doped (A) and Nd-doped (B) ceria-based samples compared to pure CeO_2, La_2O_3 and Nd_2O_3 (the bands marked with asterisks match those reported in [48]).

Concerning the defect band, it consists of a single peak for pure ceria, that was previously assigned to Frenkel anion pairs, i.e. oxygen vacancies generated by the displacement of a lattice oxide ion into an interstitial site [46,49,50]. In the presence of the rare earth dopants, the defect-induced Raman band appears broader and more intense compared to pure ceria, witnessing an increased defect density. In the case of a moderate La/Nd substitution (10%) two components can be clearly distinguished. The first one, located around 540 cm^{-1}, has been assigned to oxygen vacancies associated with the reduction of Ce^{4+} to Ce^{3+} or to the incorporation of trivalent dopants [51–54]; consistently, this peak is very intense in the case of Nd^{3+} and La^{3+} doped ceria. The second component occurs at 596 cm^{-1}, at a Raman shift roughly corresponding to the one observed for intrinsic Frenkel anion pairs, whose amount however increases in the presence of dopants [23]. Interestingly, these two peaks become less resolved at 25% doping and completely convoluted in the case of the equimolar samples. This behavior can be tentatively explained by the generation of several defect sites of the same type in different or distorted lattice environments, increasing the linewidth of the two bands until they cannot be resolved anymore. A reduction of the concentration of intrinsic oxygen-containing defects when Ce^{4+} is increasingly replaced by the 3+ dopant cations can also be hypothesized. The ratio between the area of the whole D band and the area of the F_{2g} peak can be employed as an estimation of the defect density [32,55,56]; the values of this D/F_{2g} ratio are

reported in Table 1 and evidence a significant increase of the defectiveness and oxygen deficiency of the catalysts upon rising the dopant concentration.

Moreover, the comparison of the Raman spectra of the doped catalysts with the ones of the pure La and Nd oxides shown in Fig. 4 further confirms the absence of significant dopant segregation already inferred by XRD analysis, or anyway possible clusterizations within nanometric domains are beyond the sensitivity of the techniques. Indeed, the main bands of the two rare earth oxides, which are in agreement with the previously reported vibrational pattern of hexagonal (195 and 409 cm^{-1}) La_2O_3 [57] and mixed hexagonal (190 and 436 cm^{-1}) [57] and cubic (331 cm^{-1}) [58] Nd_2O_3, are not observed in the Raman spectra of the doped ceria samples, even at 50% Nd or La concentration, evidencing a good incorporation of the dopants in ceria lattice. Moreover, the weak Raman modes marked with an asterisk in the spectrum of the pure La_2O_3 match very well the vibrational pattern of the lanthanum oxide synthesized by Cui et al. [48] and are also absent in the spectra of the doped catalysts.

3.1.2. Surface oxidation state and reducibility

The surface chemical properties of the different materials were studied via XPS. The composition of the outermost atomic layers of the mixed catalysts, in terms of dopant concentration, is reported in Table 2. At low doping, significant compositional differences were observed between bulk and surface. In fact, a higher-than-expected lanthanum content was detected at the surface of Ce90La10 and Ce75La25, while the Ce90Nd10 sample mainly accommodates Nd in the bulk. Instead, the other materials are more uniform, although a slight cerium prevalence can be observed at the surface of the two equimolar oxides.

Table 2

Composition of the six catalysts and relative abundance of the surface species obtained via XPS.

Catalyst	**Dopant content** [a] (% at.)			**Oxygen species** (%)		**Cerium species** (%)	
	Nominal	**Bulk** [b]	**Surface**	**O_α**	**O_β**	**Ce^{3+}**	**Ce^{4+}**
CeO_2	-	-	-	31.8	68.3	22.0	78.0
Ce90La10	10	9.9	24.4	51.8	48.2	31.6	68.4
Ce75La25	25	26.0	35.8	47.3	52.7	28.0	72.0
Ce50La50	50	50.0	42.4	61.7	38.3	25.4	74.6
Ce90Nd10	10	10.1	5.3	32.5	67.5	23.2	76.8
Ce75Nd25	25	24.1	26.2	38.7	61.3	22.7	77.3
Ce50Nd50	50	49.8	45.6	51.7	48.3	21.2	78.8

[a] Dopant content is expressed in percentage of La or Nd with respect to the total amount of cations
[b] Dopant content in the bulk measured via EDX

The O 1s XP spectra (displayed in Fig. S6 A) can provide information about the surface oxygen species of the six catalysts. Two distinct peaks were observed for all the samples. The lower binding energy peak, centered at 528.4 – 528.8 eV, can be ascribed to lattice oxygen (O_β), i.e. O^{2-} ions bounded to cerium [18,25,56,59–61]. In the mixed oxides, this component is slightly shifted towards lower binding energy with respect to pure ceria, as a consequence of the doping. A similar effect was previously observed in other ceria-based materials as well [25,61]. The second peak at about 531.2 eV has been instead associated with the presence of different capping oxygen species (O_α), such as hydroxyls (OH^-), carbonates (CO_3^{2-}) and also highly reactive peroxide (O_2^{2-}) or superoxide (O_2^-) ions [18,56,59,60]. The latter species can foster oxygen spillover at the surface and take part in the catalysis, hence their increase may be related to a higher soot oxidation activity [25], as also recently observed for Nd-doped ceria synthesized by glycine-nitrate-process [31]. A third low-intensity component located at 533.8 eV was detected in the Ce90La10 spectrum and it can result from the presence of adventitious species such as adsorbed water, formates or carbonates [62–64]. The relative abundance of the O_α and O_β species is reported in Table 2. All the mixed oxides exhibited a larger quantity of

capping oxygen species compared with pure ceria. Moreover, the O_α abundance generally rises with increasing dopant loading and it is higher in the La-containing samples.

In the high-resolution XP spectra of the Ce 3d core level (Fig. S6 B) two sets of features can be identified: five "v" peaks correspond to Ce $3d_{5/2}$ level, while five "u" peaks are related to the Ce $3d_{3/2}$ state. Among them, four peaks (v°, v', u° and u') can be assigned to Ce^{3+} ions, while the remaining six peaks can be ascribed to the 4+ oxidation state [18,36,64–66]. The Ce^{3+} abundance can thus be estimated through peak deconvolution, which was performed with a procedure adapted from [67]; the thus obtained values are reported in Table 2. The La-doped catalysts are characterized by a relative quantity of Ce^{3+} significantly higher than that of pure CeO_2, in line with the findings of Lee et al. [68]. Conversely, Nd addition does not affect so much this property. However, the Ce^{3+} relative abundance decreases at increasing dopant content for both La and Nd. Therefore, a mild doping promotes the formation of Ce^{3+} ions, while the latter species become less favored as the dopant content further increases.

The La 3d and Nd 3d XP spectra of the doped catalysts are compared with the ones of pure La_2O_3 and Nd_2O_3 in Fig. S7. Lanthanum oxide exhibits two main peaks related to the La $3d_{5/2}$ and La $3d_{3/2}$ levels, which are located at 834.9 and 851.7 eV, respectively, in agreement with previous literature [69,70]. The spin-orbit splitting of 16.8 is characteristic of the La_2O_3 phase [71,72]. Other two satellite peaks and two La LMM Auger signals are visible as well [69]. The XP spectra of La-doped ceria feature two additional peaks at about 832.6 and 849.5 eV, which could be due to the La incorporation in ceria lattice or to La bonded to OH or other O_α species [73]. Nd_2O_3 exhibits two main and two satellite peaks in the XP spectrum as well [74,75]. The main peaks are located at 982.5 and 1005 eV for the Nd $3d_{5/2}$ and $3d_{3/2}$ states, respectively, and the spin-orbit splitting of 22.5 eV is typical of this oxide [72]. An additional peak at high binding energy has been ascribed to an O KLL signal [74,75]. The three Nd-doped catalysts are characterized by similar XP spectra, with the Nd 3d peaks slightly shifted towards lower binding energy.

The reducibility of the catalysts was examined through H_2-TPR and the obtained curves are shown in Fig. 5 A and B. The profile of pure ceria features two peaks since its reduction occurs in two steps. The lower temperature peak located around 600 °C is related to the reduction of superficial Ce^{4+} ions, while the larger band above 700 °C is the result of the progressive release of lattice oxygen from the bulk at very high temperature [34,76]. The doped catalysts are characterized by similar curves, but with surface reduction peaks slightly anticipated at lower temperatures. The only exception is represented by Ce50Nd50, which also exhibited an intense peak between 600 and 700 °C, suggesting that a significant part of the subsurface of this sample may be reduced almost simultaneously with the surface.

Generally, the incorporation of dopant ions in the ceria lattice can weaken the cerium-oxygen bonds and induce the formation of oxygen vacancies, fostering oxygen mobility and thus promoting the reducibility of the mixed oxides [32,43,44]. However, for the considered set of catalysts the beneficial effects of doping seem to be limited to the slight anticipation of the surface reduction at lower temperature. Instead, the quantity of oxygen released was not positively affected by La or Nd addition, as pointed out by the values of H_2 consumption during TPR reported in Table 3. In detail, the specific consumption of hydrogen related to surface reduction generally decreased when adding La or Nd, in agreement with the XPS data. In fact, two phenomena occur simultaneously at the catalyst surface when the dopant content is raised from 10% to 50%: i) the relative quantity of cerium ions decreases and ii) the fraction of Ce^{4+} among the cerium ions increases (Table 2). As a whole, the first effect prevails on the second one, thus the total quantity of Ce^{4+} ions at the surface decreases as the dopant loading increases. The loss of reducible species upon doping accounts for the gradual decrease of the specific H_2 consumption related to surface reduction in the mixed oxides. Only the Ce50Nd50 showed a higher consumption of hydrogen at low temperature with respect to pure ceria, due to an improved subsurface reduction. However, the global H_2 consumption at the end of TPR gradually decreased at increasing dopant loading and was minimum for the two equimolar oxides. This trend is likely due to the absence of a redox cycle of La or Nd, whose addition is therefore related to a lower quantity of oxygen which can be extracted by hydrogen, consistently with the higher oxygen deficiency revealed by Raman spectroscopy. However, if the H_2 consumption is normalized to the amount of ceria in the mixed oxide, it is maximum for the two equimolar mixtures and minimum for 10% doped ceria, confirming the weakening of the cerium-oxygen bonds upon dopant addition.

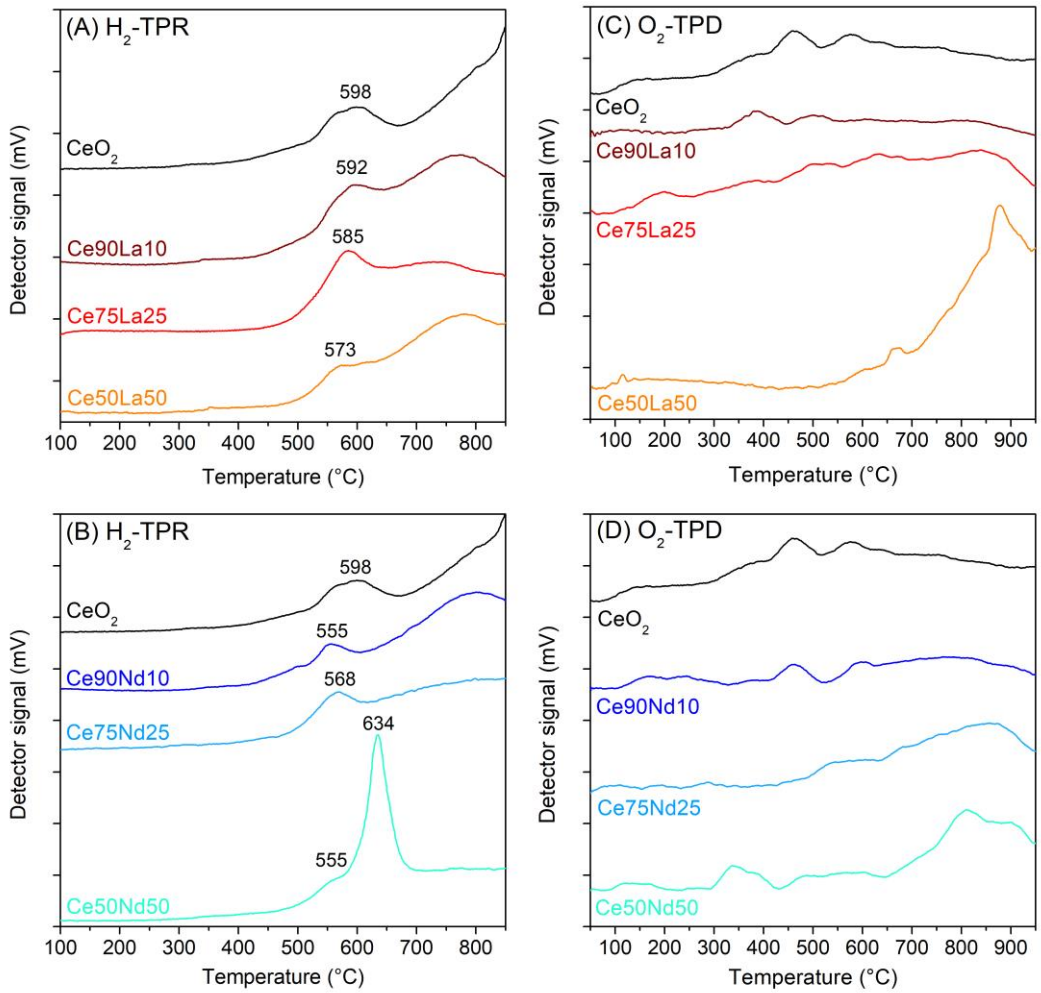

Fig. 5. H_2-TPR (A, B) and O_2-TPD (C, D) profiles of the La-doped and Nd-doped samples compared with pure ceria.

Table 3

Specific consumption of hydrogen during H_2-TPR.

Catalyst	**Superficial H_2 consumption** ($mmol\ g_{catalyst}^{-1}$)	**Total H_2 consumption**	
		($mmol\ g_{catalyst}^{-1}$)	($mmol\ g_{ceria}^{-1}$)
CeO_2	0.441	1.77	1.77
Ce90La10	0.442	1.17	1.30
Ce75La25	0.431	1.19	1.59
Ce50La50	0.341	1.03	2.06
Ce90Nd10	0.380	1.25	1.39
Ce75Nd25	0.397	1.18	1.57
Ce50Nd50	0.637	0.98	1.96

The oxygen release was further investigated through O_2-TPD, whose results are reported in Fig. 5 C and D. In this case, the oxygen transfer and the related TCD signal are much lower than those recorded during H_2-TPR, since oxygen desorption is only promoted by the temperature. Lowly doped samples exhibited profiles similar to that of pure ceria, characterized by the presence of some minor desorption peaks in the 300 – 600 °C temperature range [77]. A high

loading of La or Nd was instead associated with an increase in the quantity of oxygen desorbed above 600 °C. This behavior is likely due to the smaller crystals and higher surface area typical of the highly doped oxides. In particular, an intense peak at high temperature can be observed in the case of Ce50La50, which may be related to the remarkably high abundance of O_α species at the surface of this sample, as found out via XPS.

3.1.3. Acid-base properties of the surface

Besides reducibility and oxygen availability, the acid-base properties of the surface are also of interest since they affect the strength of interaction between the catalyst and various gaseous reactive species. The oxidizing activity is hence linked to the material acidity [78,79]. For this reason, the acid and basic sites of the mixed oxides were investigated via NH_3-TPD and CO_2-TPD, respectively; the desorption profiles obtained are displayed in Fig. 6.

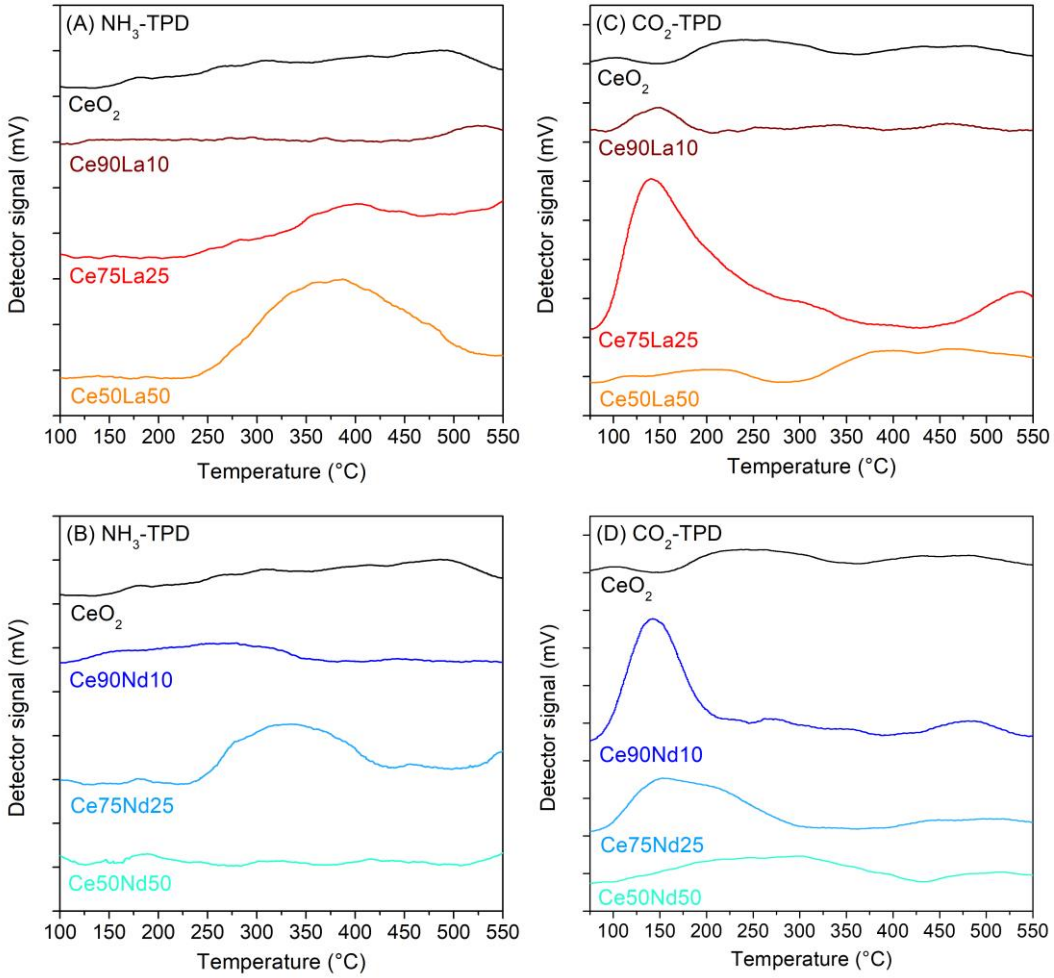

Fig. 6. NH_3-TPD (A, B) and CO_2-TPD (C, D) profiles of the La-doped and Nd-doped samples compared with pure ceria.

Concerning NH_3-TPD, pure ceria is characterized by an almost flat line, which suggests the absence of significant quantities of acid sites; this is consistent with the mainly basic nature attributed to this oxide [80,81]. Similarly, some doped samples show flat profiles too, as can be seen in Fig. 6 A and B. Instead, quite intense ammonia desorption bands between 250 and 500 °C can be clearly observed for Ce50La50 and Ce75Nd25, signaling the presence of acid sites with a medium strength at the catalyst surface [82,83]. These sites are stronger and more abundant for the Ce-La equimolar oxide (see Table S1 for the site density calculation). A less intense band attributable to quite strong acid sites could be detected for the Ce75La25 sample as well.

In line with previous studies [25,84,85], the quantity of basic sites was affected by La and Nd doping too, as evinced by CO_2-TPD. In fact, the profiles in Fig. 6 C and D point out the presence of a considerable amount of weak sites in the lowly doped samples, revealed by the desorption peaks at low temperature, while these sites were much less in pure

ceria and in the two equimolar mixtures. However, the latter samples were characterized by significant CO_2 desorption above 300 °C. Actually, CO_2 adsorption on metal oxides can occur on sites with various strength, e.g. superficial OH, O^{2-} or cations, resulting in the formation of different carbonaceous species such as hydrogen carbonates, mono/bi/poly-dentate carbonates or metal carboxylates [80,86]. The peak located at about 150 °C, which is remarkably intense for the Ce75La25, Ce90Nd10 and Ce75Nd25 samples, has been ascribed to the decomposition of monodentate carbonates. The large band around 400 – 500 °C could instead signal the presence of quite stable bidentate and polydentate carbonates on the Ce50La50 catalyst [80].

3.2. Catalytic activity

The catalytic activity of the prepared materials was investigated considering three reactions which play a key role in the field of automotive aftertreatment, namely CO, NO and soot oxidation.

3.2.1. CO oxidation

The catalytic activity towards CO oxidation was assessed in isothermal mode, considering a sequence of steady states at different temperatures; in this way, possible adsorption or desorption phenomena do not affect the analysis. The profiles of CO conversion as a function of the temperature are presented in Fig. 7, while the temperatures at which 10%, 50% and 90% of CO conversion were reached ($T_{10\%}$, $T_{50\%}$ and $T_{90\%}$, respectively) are reported in Table 4.

Moderate doping allows to fairly improve the CO oxidation activity with respect to pure ceria: in fact, the $T_{50\%}$ reduces by ca. 25 and 90 °C upon the introduction of 10% of La and Nd, respectively. This variation can be ascribed to the formation of a proper quantity of defect sites, associated with Ce-O bonds weakening. However, further increases of the dopant quantity result in a gradual worsening of the catalytic performances, with the Ce-La and Ce-Nd equimolar oxides presenting a $T_{50\%}$ about 20 and 65 °C higher than that of pure ceria. Consistently, also the values of the specific reaction rate of CO oxidation (r_{CO}), reported in Table 4, point out a reverse trend between dopant loading and catalytic activity.

Such an effect may be linked to the greater presence of strong basic sites in highly doped ceria, as revealed by CO_2-TPD: CO and CO_2 might indeed accumulate on these sites, forming stable carbonate-like species which can hamper the adsorption of further CO molecules at the catalyst surface, thus retarding CO conversion [25,84]. The transformation of carbonates into physisorbed CO_2 has also been recognized as the rate determining step (RDS) in the carbonate-mediated MvK mechanism of CO oxidation over rare earth-doped ceria (111) facets [87]; stronger basic sites can be therefore expected to increase the RDS energy barrier, detrimentally affecting the CO oxidation rate. Furthermore, excessive ceria dilution likely contribute to the observed activity decay: in fact, since the 3+ dopant ions cannot be oxidized, an over-reduced material presenting a lower density of MvK active sites is obtained upon high dopant loading, consistently with the Raman and H_2-TPR results. For these reasons, higher surface area and defect abundance do not always seem to improve the catalytic activity in the case of CO oxidation over rare earth-doped ceria.

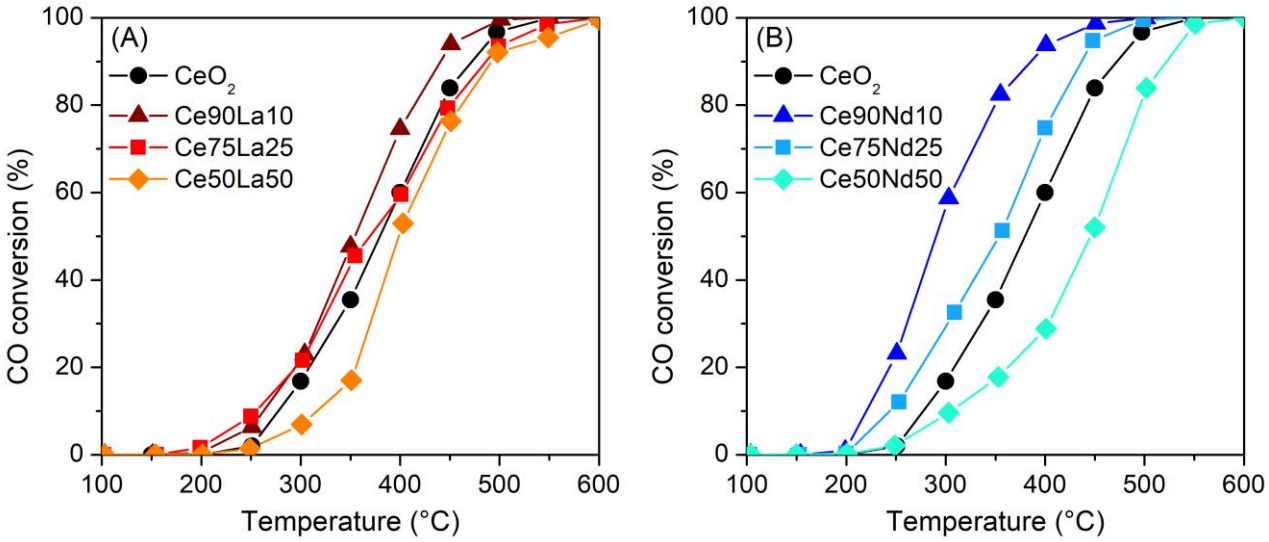

Fig. 7. Evolution of the CO conversion as a function of the temperature during the CO oxidation tests performed on the La-doped (A) and Nd-doped (B) samples.

3.2.2. NO oxidation

NO oxidation tests were carried out in isothermal mode too, in order to avoid possible adsorption or desorption phenomena. The results are reported in Fig. 8, which displays the profiles of the NO_2 fraction in the NO_x mixture downstream the reactor as a function of the temperature.

Pure ceria starts promoting NO to NO_2 oxidation above 350 °C and reaches the maximum conversion around 450 °C, then the NO_2 fraction gradually decreases following the thermodynamic equilibrium existing between NO and NO_2 [21,88]. Despite the higher surface area, the doped samples were characterized by catalytic performances more or less similar to those of CeO_2. Actually, Ce90La10 exhibited a lower light-off temperature and a slightly higher maximum conversion at 450 °C. However, a further increase of the La loading caused a progressive drop of the catalytic activity for NO oxidation. The three Nd-doped oxides showed instead similar profiles, and only Ce75Nd25 was able to slightly outperform pure ceria in terms of maximum conversion. Therefore, La and Nd addition does not seem to significantly promote NO oxidation, probably because of the limited effects of doping on the catalyst reducibility.

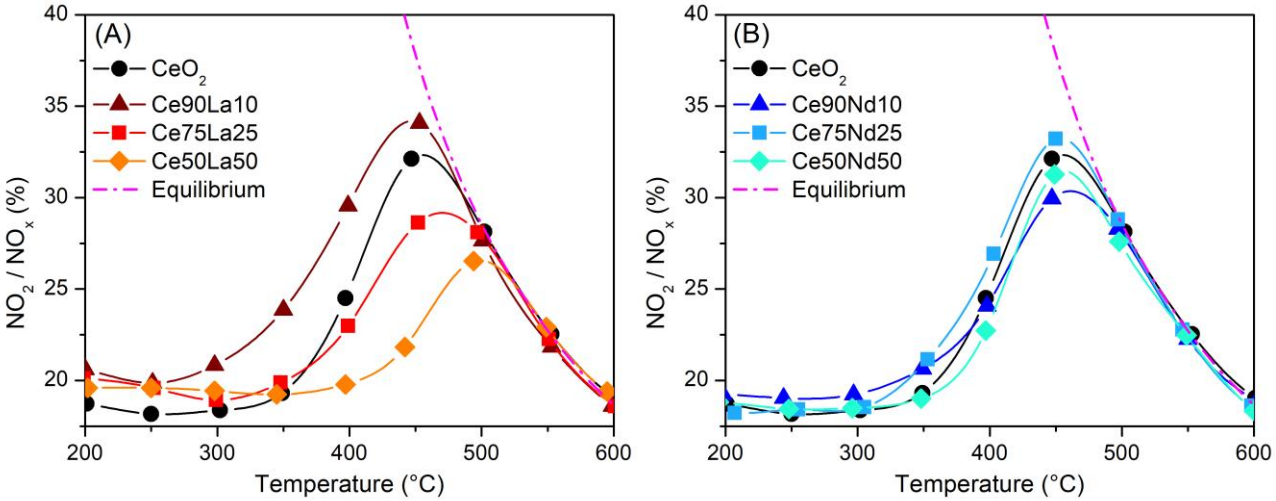

Fig. 8. Evolution of the NO_2/NO_x fraction in the outlet as a function of the temperature during the NO oxidation tests performed on the La-doped (A) and Nd-doped (B) samples.

3.2.3. Soot oxidation

The catalytic activity towards soot oxidation was carefully evaluated by performing tests in various conditions. Two different degrees of contact between the catalyst and soot powders were probed and the effects of the presence of NO_x and water were also examined. The $T_{10\%}$, $T_{50\%}$ and $T_{90\%}$ measured during the different tests are reported in Table 4 and 5 for comparison purposes.

Table 4

Summary of the results obtained from the catalytic tests of CO oxidation and of standard soot oxidation (10% O_2 in N_2) performed in different contact conditions (loose or tight contact).

Catalyst	CO oxidation				Soot oxidation						
					Loose contact			Tight contact			
	$T_{10\%}$ (°C)	$T_{50\%}$ (°C)	$T_{90\%}$ (°C)	r_{CO} at 250 °C (µmol h^{-1} m^{-2})	$T_{10\%}$ (°C)	$T_{50\%}$ (°C)	$T_{90\%}$ (°C)	$T_{10\%}$ (°C)	$T_{50\%}$ (°C)	$T_{90\%}$ (°C)	r_{soot} at 375 °C (mmol h^{-1} g^{-1})
CeO_2	277	380	472	3.50	491	574	624	419	467	504	1.31
Ce90La10	263	354	441	8.58	490	585	633	404	447	496	2.63
Ce75La25	255	370	486	7.71	434	531	606	395	442	499	3.58
Ce50La50	316	399	492	0.95	414	487	580	358	392	443	30.3
Ce90Nd10	220	290	386	28.4	474	568	612	428	479	542	1.07
Ce75Nd25	244	354	437	10.8	453	539	609	384	428	475	6.95
Ce50Nd50	305	446	522	2.15	470	559	613	412	458	526	1.95

Table 5

Summary of the results obtained from the catalytic tests of soot oxidation performed in different contact conditions (loose or tight contact) in the presence of NO_x (550 ppm NO + 10% O_2 in N_2) or water (10% H_2O + 10% O_2 in N_2).

Catalyst	In the presence of NO_x						In the presence of H_2O		
	Loose contact			Tight contact			Loose contact		
	$T_{10\%}$ (°C)	$T_{50\%}$ (°C)	$T_{90\%}$ (°C)	$T_{10\%}$ (°C)	$T_{50\%}$ (°C)	$T_{90\%}$ (°C)	$T_{10\%}$ (°C)	$T_{50\%}$ (°C)	$T_{90\%}$ (°C)
Ce90La10	444	531	596	-	-	-	-	-	-
Ce75La25	425	505	559	-	-	-	-	-	-
Ce50La50	372	424	493	366	407	461	375	444	532
Ce90Nd10	438	526	600	-	-	-	-	-	-
Ce75Nd25	402	472	529	398	452	503	398	470	532
Ce50Nd50	439	524	588	-	-	-	-	-	-

First of all, soot oxidation was carried out in tight contact, i.e. mixing soot and catalyst via ball milling; thereby, numerous contact points between the two solid powders were created and so the catalytic performances were mainly determined by the intrinsic activity of the materials. The profiles of the CO and CO_2 produced during these tests are displayed in Fig. S8 while the conversion curves are reported in Fig. 9 A and D. As can be seen from the latter pictures and from the specific reaction rates (r_{soot}) reported in Table 4, the catalytic activity varies following this trend: Ce90Nd10 < CeO_2 < Ce50Nd50 < Ce90La10 < Ce75La25 < Ce75Nd25 < Ce50La50. Although Ce90Nd10 seems

slightly less active than pure CeO_2, La and Nd doping generally promotes soot oxidation. In detail, two promising materials can be distinguished from the other ones. Ce75Nd25 is the most performing sample in the Nd-doped set and it was able to lower the reaction light-off temperature by 40 °C with respect to pure ceria. However, the Ce50La50 equimolar mixture exhibited the highest catalytic activity, remarkably outperforming all the other oxides. This sample was indeed able to convert more than half of the soot initially present below 400 °C.

A correlation can be found between the catalytic activity and the surface acidity: indeed, it is worth noting that the three most active catalysts are the ones presenting more acid sites at their surface, as previously pointed out by NH_3-TPD (section 3.1.3). Actually, the presence of strong acid sites can foster the formation of carbon radical intermediates, thanks to the electronic interactions at the interface between soot and catalyst particles [89,90]. The thus formed highly reactive species can be easily oxidized by oxygen coming from both the gas bulk or the catalyst lattice and this mechanism likely contributes to an effective conversion of soot at lower temperature. The superficial oxygen species (O_α), which are especially abundant over the Ce50La50 sample, can also be expected to play a primary role in soot oxidation: indeed, the ability to generate and release active oxygen has been recognized as a crucial factor for the activity of La-doped ceria in the works of Katta et al. and Bueno-López et al [28,29].

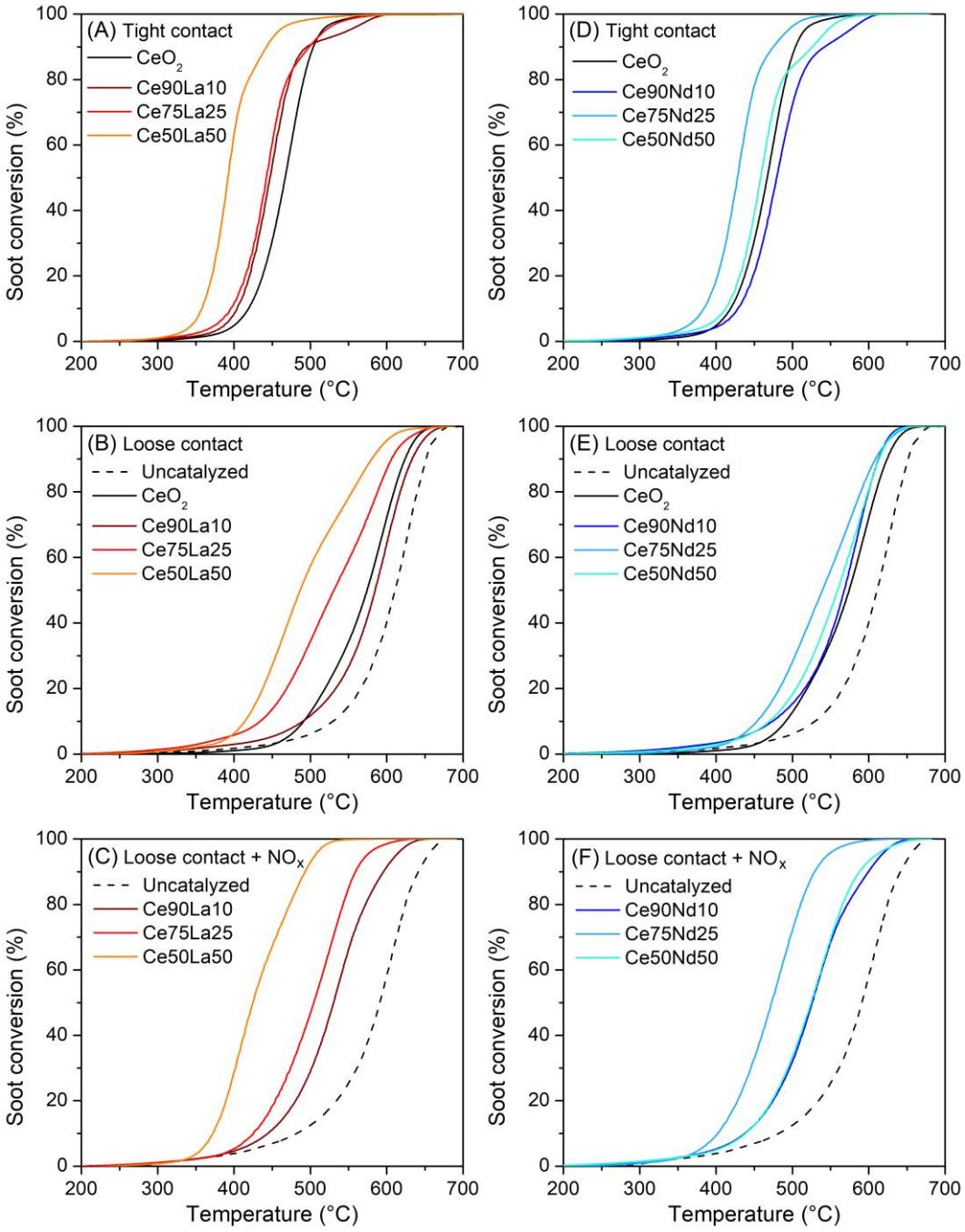

Fig. 9. Conversion curves as a function of the temperature resulting from the different soot oxidation tests performed on La-doped (A, B, C) and Nd-doped (D, E, F) ceria. NO_x-free soot oxidation was performed in tight (A, D) and loose (B, E) contact, while NO_x-assisted soot oxidation was carried out in loose contact (C, F).

Moreover, the selectivity towards CO_2 was also assessed and the values obtained are reported in Fig. S9. Ce50La50 resulted to be the most selective mixed oxide, although its CO_2 selectivity (93.5%) was slightly lower than that of pure ceria (97.1%); Ce50Nd50 was instead the least selective (89.7%). The higher CO production observed for the doped materials is likely related to the negative effects of La and Nd addition on ceria catalytic activity towards CO oxidation. It is however worth noting that all the samples presented a much higher CO_2 selectivity with respect to the uncatalyzed case, in which it was only 61.4%.

Fig. 9 B and E display the results of the soot oxidation tests carried out in loose contact, while direct comparisons between the performances in tight and loose contact are reported for each sample in Fig. S10. As expected, in loose contact all the conversion curves are shifted towards higher temperatures. Actually, in this case the transfer of active oxygen species from the catalyst to the soot particles is hindered by the lower amount of contact points [15,44,91]. Furthermore, a wider range of temperature is required for the complete oxidation, since different fractions of soot with different intensities of contact with the catalyst coexist in the solid mixture [92,93]. If the $T_{50\%}$ are considered (Table 4), the catalytic activity in loose contact follows the trend: Ce90La10 < CeO_2 < Ce90Nd10 < Ce50Nd50 < Ce75Nd25 < Ce75La25 < Ce50La50. Pure ceria and the lowly-doped samples are again characterized by similar performances, while a higher dopant loading is associated with a better activity, especially in the case of the Ce-La mixed oxides. La doping also caused a progressive increase of the specific reaction rate, whose values calculated at 400 °C are reported in Table 6. Instead, Ce75Nd25 was again the most active among the Nd-doped samples.

Table 6

Specific reaction rates of soot oxidation (r_{soot}) during the catalytic tests performed in loose contact in the absence (10% O_2 in N_2) and in the presence (550 ppm NO + 10% O_2 in N_2) of NO_x.

Catalyst	**r_{soot} at 400 °C** ($\mu mol\ h^{-1}\ m^{-2}$)	
	Loose contact	**Loose contact + NO_x**
CeO_2	67.8	-
Ce90La10	71.5	241
Ce75La25	86.9	156
Ce50La50	230	858
Ce90Nd10	74.2	85.1
Ce75Nd25	81.4	392
Ce50Nd50	69.1	137

These results could be correlated with the different morphologies, since the catalysts presenting more fibers are also characterized by a higher ability in oxidizing soot, in accordance with previous studies [16,44,94]. In fact, a network of rods and fibers can suitably accommodate soot particles maximizing the number of contact points [16]. Moreover, the decrease of the temperature required for soot combustion is related to the reduction of the particle size upon doping, as displayed in Fig. 10. The Ce50La50 sample is the most performing catalyst in loose contact, too: thanks to its high intrinsic activity and its fibrous structure, this equimolar oxide was indeed able to reduce the temperature required for ceria-catalyzed soot oxidation by about 80 °C, with a $T_{50\%}$ of 487 °C. Of course, the greater abundance of capping oxygen species and acid sites at the surface and the higher specific surface area contribute to the excellent catalytic properties of this material as well.

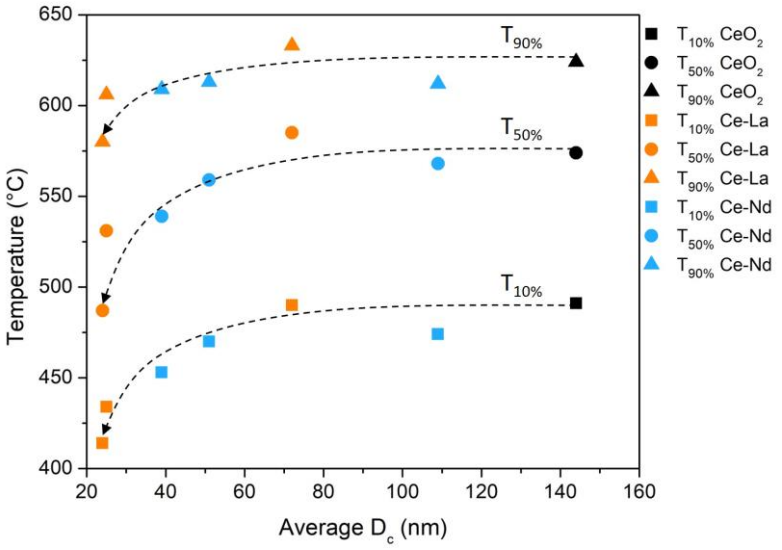

Fig. 10. Variation of the catalytic performances as a function of the average crystallite size of the samples during soot oxidation in loose contact (the average of the two different D_C values was used for La-doped ceria, Ce75Nd25 and Ce50Nd50).

In order to check the stability of the catalysts, the Ce50La50 and Ce75Nd25 samples were subjected to an aging treatment at 700 °C for 8 h. This procedure only marginally affected the structural properties of the mixed oxides, inducing a very slight growth of the average crystal size (few nanometers) and an associated decrease of the specific surface area (as further detailed in Fig. S11 and Table S2). Consistently, the soot oxidation performances were almost unaffected by aging and very similar conversion curves were obtained after the high temperature treatment (Fig. S12), indicating that these two active samples are highly stable.

Moreover, the effect of water on the soot oxidation performances of these materials was also evaluated, since a high quantity of this species is usually present in the engine exhaust. As can be seen in Fig. S13 and Table 5, the addition of 10% H_2O in the reactant gas phase beneficially affects loose contact soot oxidation, lowering the T_{50} by more than 40 °C. Such a promoting effect, previously observed for other ceria-based materials [95,96], is probably the result of different phenomena. Actually, surface hydroxylation can improve oxygen mobility while a wet soot-catalyst interface can account for a more effective oxygen transfer [97,98]. Moreover, Park et al. have recently found out via isotopic experiments and DFT studies that water can behave as an active oxygen source for soot oxidation [96]; in fact, H_2O can easily adsorb and dissociate over Ce-based oxides, forming reactive OH species which can significantly increase the reaction rate.

3.2.4. NO_x-assisted soot oxidation

The soot oxidation tests in loose contact were repeated in the presence of NO_x and the conversion profiles are displayed in Fig. 9 C and F. A direct comparison between the results obtained in the presence and in the absence of NO_x is instead reported in Fig. S14. The NO fed to the reactor can be partly converted to NO_2 by the catalyst; the latter species is a stronger oxidant than O_2, therefore able to promote soot combustion [19,88,99]. In fact, the performances of all the samples benefitted from NO addition, as all the conversion curves are shifted towards lower temperature when soot oxidation is assisted by NO_x. In this case, the trend of catalytic activity is the following: Ce50La50 > Ce75Nd25 > Ce75La25 > Ce50Nd50 ≈ Ce90Nd10 ≈ Ce90La10 (Table 5). A slightly different trend can be observed considering the specific reaction rates reported in Table 6. In any case, Ce50La50 and Ce75Nd25 confirm to be the most active samples for soot oxidation.

The investigation of the catalytic mechanisms promoted by mixed oxides during NO_x-assisted soot oxidation is a rather tough operation; indeed, several different reactions, giving rise to a complex network of interconnected pathways, are expected to take place at the same time [20,21,27,30,88,99,100]. Actually, many oxygen species can be involved in soot combustion, such as gaseous O_2, lattice oxygen ions with a MvK-like behavior or reactive oxygen species at the catalysts surface [17,18,23,24,101,102]. Furthermore, NO_x can also take part in catalytic soot oxidation and two main mechanisms have been identified. An indirect pathway involves NO oxidation over the catalyst, producing NO_2 molecules which then attack soot from the gas phase (homogeneous mechanism) [19,20]; at the end, NO is obtained

again and the whole cycle may be repeated [21,103]. Besides, soot oxidation can also occur via a direct pathway involving the NO_x adsorbed on the catalyst (heterogeneous mechanism): in fact, nitrites or nitrates at the solid surface can decompose in the proximity of soot particles, generating active species able to attack soot directly from the solid phase [21,99]. The significance of each mechanism depends on various factors, such as the chemical properties of the catalyst or the operative conditions. For instance, the indirect mechanism has been recognized as the predominant one when noble metals such as Pt are employed [27,103]. However, metal oxides are usually less active towards NO oxidation and so their catalytic performances may be related to the activation and promotion of other pathways. For example, a direct mechanism involving the adsorbed nitrates has been recently proposed for nanostructured equimolar ceria-praseodymia [21].

In order to shed some light on the catalytic mechanisms favored by La- and Nd-doped ceria and to verify if the adsorbed NO_x play a direct role in the catalysis, NO_x-assisted soot oxidation was also performed in tight contact. The thus obtained conversion curves can be compared with those previously provided by all the other soot oxidation tests; such a comparison is reported in Fig. 11 for the two most active samples, i.e. Ce50La50 and Ce75Nd25. As can be seen from the picture, the equimolar Ce-La mixture was always characterized by superior performances. Anyway, both the catalysts exhibited analogous changes when the conditions were varied. In details, NO_x addition had a remarkable promoting action on soot combustion in loose contact, while its effect was slightly detrimental in tight contact, as pointed out by the arrows in Fig. 11.

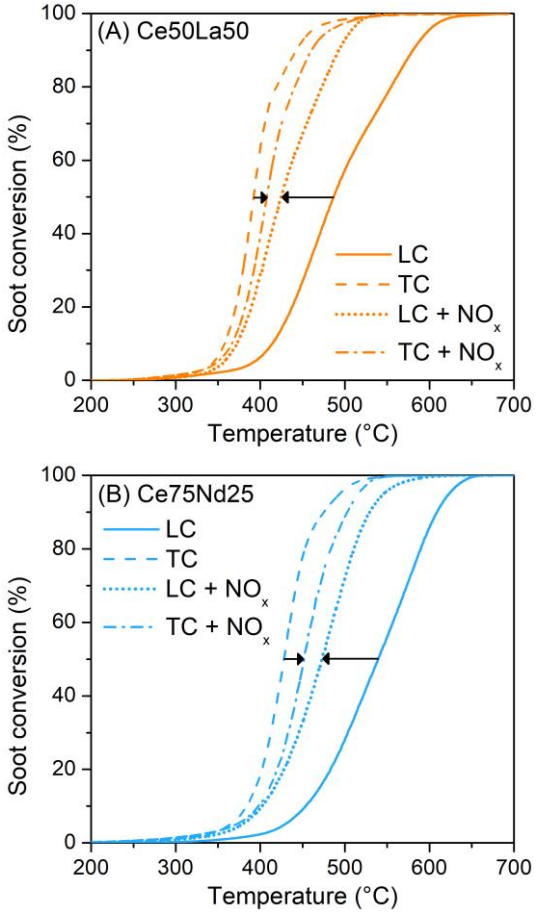

Fig. 11. Conversion curves as a function of the temperature resulting from the different types of soot oxidation tests performed on the Ce50La50 (A) and Ce75Nd25 (B) samples in loose contact (LC) or tight contact (TC) in the absence or in the presence of NO_x. The arrows highlight the effects of NO_x addition on soot conversion.

An explanation for this behavior should take into account all the mechanisms presented above. Consistently, a simplified scheme describing some of the possible phenomena involved is depicted in Fig. 12 for the Ce50La50 sample. Actually, in loose contact the low number of contact points is a kinetic limitation, since the transfer of active oxygen species can only take place in those regions of the catalyst surface which are close to soot particles (Fig. 12 A). In this

situation, the presence of NO is beneficial: indeed, it can be converted to NO_2 which can then move through the gas phase and reach soot regardless of the degree of contact (Fig. 12 C). Conversely, in tight contact the reaction kinetics is controlled by the intrinsic activity of the species involved in soot oxidation. Reactive oxygen species, which are believed to be more powerful oxidizers than NO_2 [88,99], are far available thanks to the intimate contact conditions (Fig. 12 B). In this context, the presence of NO_x can lower the activity of the catalyst, since adsorbed nitrites or nitrates may replace the highly active oxygen species at the surface and hamper their re-formation (Fig. 12 D). In fact, since soot oxidation in tight contact starts at a lower temperature (below 400 °C), adsorbed NO_x may be quite stable in these conditions [104], thus lowering the overall reaction rate; moreover, the presence of strong basic sites at the Ce50La50 surface also accounts for enhanced nitrates stability.

Concerning the Ce75Nd25 sample, NO_x adsorption should be less significant, due to the lack of strong basic sites. However, gaseous NO may still consume part of the reactive oxygen species available at the catalyst surface; if this competitive effect prevails over the promoting action of the thus generated NO_2, it can result in retarded soot oxidation.

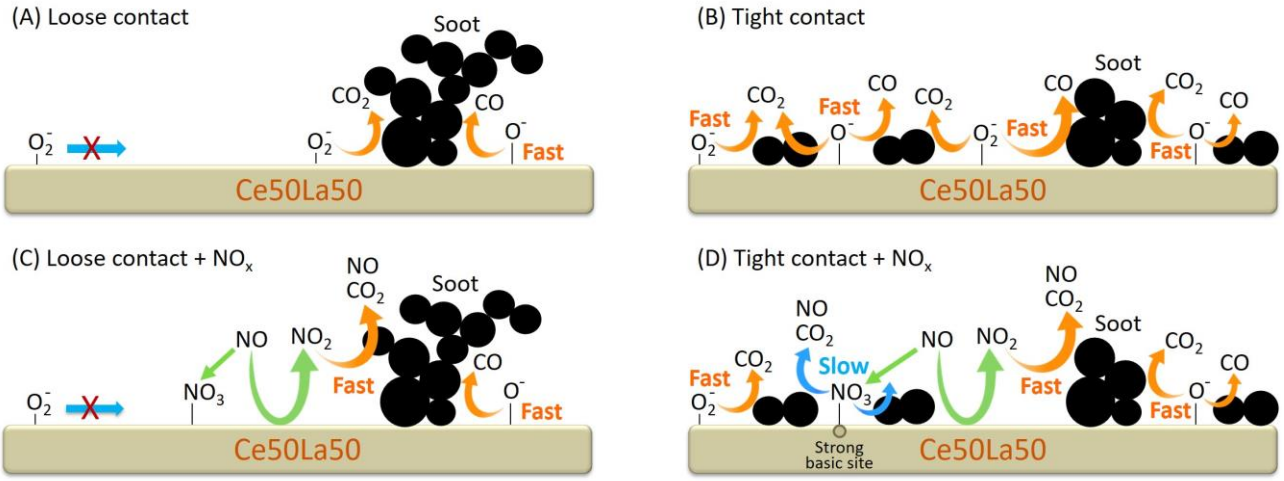

Fig. 12. Scheme reporting some of the possible reaction pathways occurring at the surface of the Ce50La50 catalyst during soot oxidation in the absence (A, B) or in the presence (C, D) of NO_x in loose (A, C) or tight (B, D) contact.

3.2.5. Comparison among ceria dopants: La and Nd vs Pr

Different studies have been devoted to comparing various dopants for ceria-based catalysts [25,32,53]. For instance, Katta et al. compared Zr and La as ceria promoters, concluding that La doping is associated with better thermal stability and enhanced soot oxidation activity [28]. Here, for the sake of completeness, the catalytic properties of La- and Nd-doped ceria will be compared with those of similar Pr-doped catalysts, which have shown very interesting performances for soot oxidation [44]. Such a comparison can be found in Fig. 13, which reports the $T_{50\%}$ measured during soot oxidation in tight and loose contact as a function of dopant loading for ceria doped with the three different lanthanides. As can be seen, La has a progressive beneficial effect on ceria activity and it is the most effective dopant at high loading.

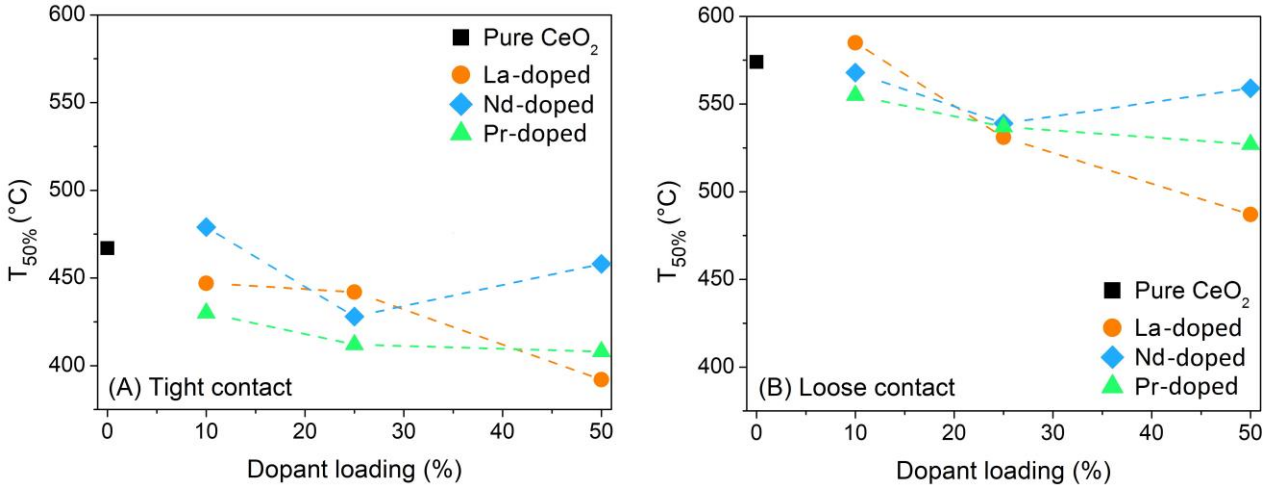

Fig. 13. Catalytic performances (in terms of $T_{50\%}$) as a function of dopant loading during soot oxidation performed in tight (A) and loose (B) contact. The La- and Nd-doped samples are compared to other nanostructured ceria-based oxides obtained via hydrothermal procedure and tested in analogous conditions, but containing Pr [44].

In fact, Ce50La50 was even able to outperform equimolar ceria-praseodymia (Ce50Pr50), which has been recognized as one of the most promising ceria-based catalysts for soot oxidation [22,26]. A direct comparison of the soot conversion curves of Ce75Nd25 and Ce50La50 with that of an analogously synthesized and tested Ce50Pr50 sample can be found in Fig. S15, which confirms the higher activity of Ce50La50 (for further information about ceria-praseodymia, see Fig. S16 and S17). The different redox and acid-base properties of the mixed oxides can account for the different activities. La-doping provides ceria surface with a greater amount of strong acid sites, as can be observed in Fig. 14 A and Table 7, promoting soot oxidation as discussed above. However, Ce50Pr50 can partially compensate for the lower quantity of medium and strong acid sites thanks to the advantages connected to the $Pr^{3+} – Pr^{4+}$ redox cycle. In fact, Pr addition is associated with an improved reducibility (H_2-TPR reported in Fig. 14 C) and with the formation of active oxygen vacancies, which can act as MvK sites during the oxidation reactions [44].

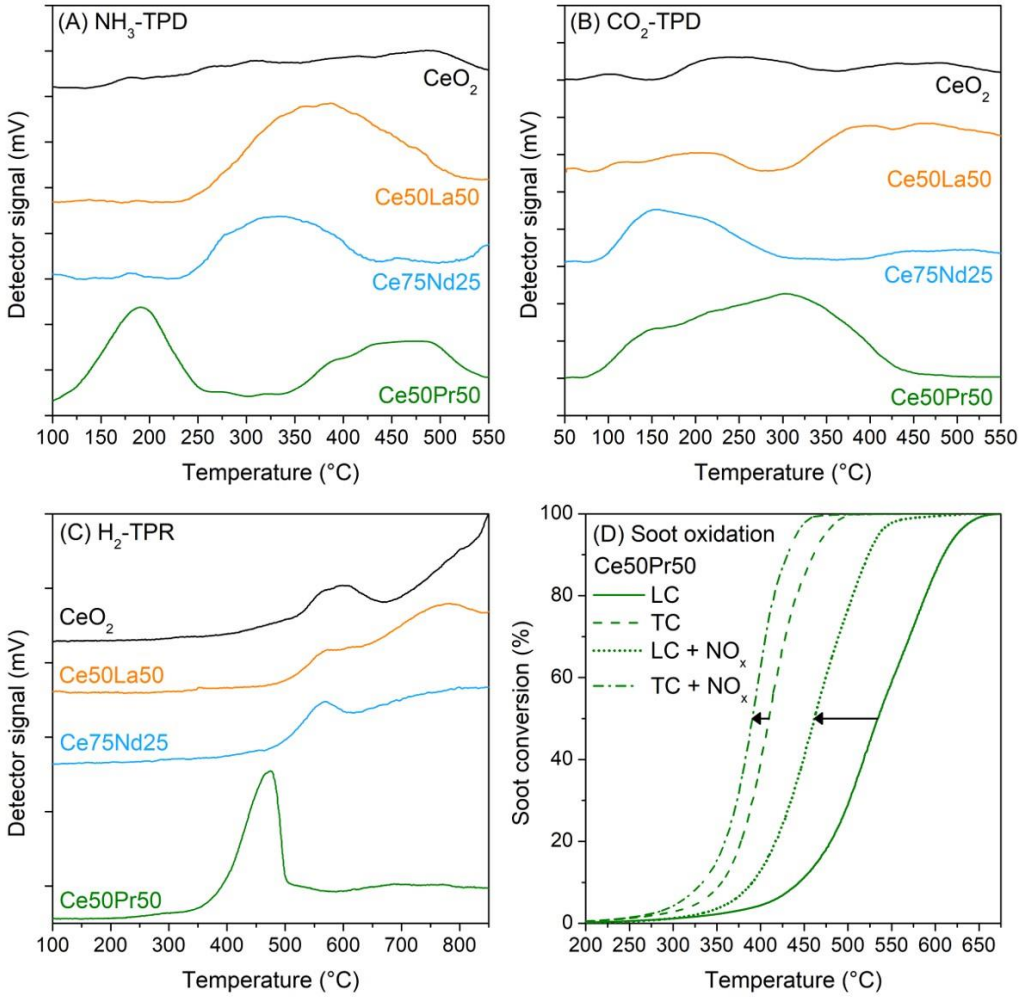

Fig. 14. Comparison of the NH_3-TPD (A), CO_2-TPD (B) and H_2-TPR (C) profiles of pure ceria, Ce50La50, Ce75Nd25 and Ce50Pr50. Conversion curves (D) resulting from the different types of soot oxidation tests performed on Ce50Pr50 in loose contact (LC) or tight contact (TC) in the absence or in the presence of NO_x; the arrows highlight the effects of NO_x addition on soot conversion.

Consistently, the Raman spectrum of Pr-doped ceria features an intense defect band (Fig. S18), which signals the presence of numerous defects. However, a direct comparison among the D/F_{2g} ratio of Ce50Pr50 (1.49) and those of the other samples (reported in Table 1) may not be reliable, since different effects can contribute to the high value obtained for ceria-praseodymia. First, a defect-related component at 570 cm^{-1}, which has been ascribed to the symmetric stretching mode of sites containing Pr^{4+} ions and oxygen vacancies, is characterized by resonance Raman effect [105], i.e. by an enhanced Raman signal. Secondly, the higher light absorption of Pr-doped ceria results in a lower penetration depth: a more superficial region is hence investigated, which is usually richer in defects with respect to the oxide bulk [106]. Nevertheless, the structural behavior of the different samples was further investigated by performing in situ Raman measurements during soot oxidation (the spectra acquired at different temperatures are reported in Fig. S19). An interesting comparison can be made between the RT Raman spectra collected on fresh sample and those recorded on the spent catalyst at the end of the in situ test. As can be noticed in Fig. 15, the mixed oxides containing La or Nd have a quite static structure and are characterized by a stable D/F_{2g} ratio. Instead, an increase of the latter parameter and of the defect band was observed for Ce50Pr50 after soot oxidation, pointing out the more dynamic and flexible structure of this catalyst.

Table 7

Density of acid and basic sites (expressed as probe molecule adsorption capacity per unit of catalyst surface area) estimated from NH_3-TPD and CO_2-TPD. The desorption profiles were fitted using gaussian curves and the peaks were

ascribed to weak, medium, or strong sites when falling in the 100 – 250 °C, 250 – 400 °C, or 400 – 550 °C temperature range, respectively.

Catalyst	**Density of acid sites** (µmol of NH_3 m^{-2})			**Density of basic sites** (µmol of CO_2 m^{-2})		
	Weak	Medium	Strong	Weak	Medium	Strong
CeO_2	0.9	2.3	3.8	0.8	1.7	1.6
Ce50La50	-	5.9	6.4	1.2	1.5	3.5
Ce75Nd25	-	6.0	2.3	4.9	0.8	1.1
Ce50Pr50	5.7	1.9	5.8	4.6	6.8	-

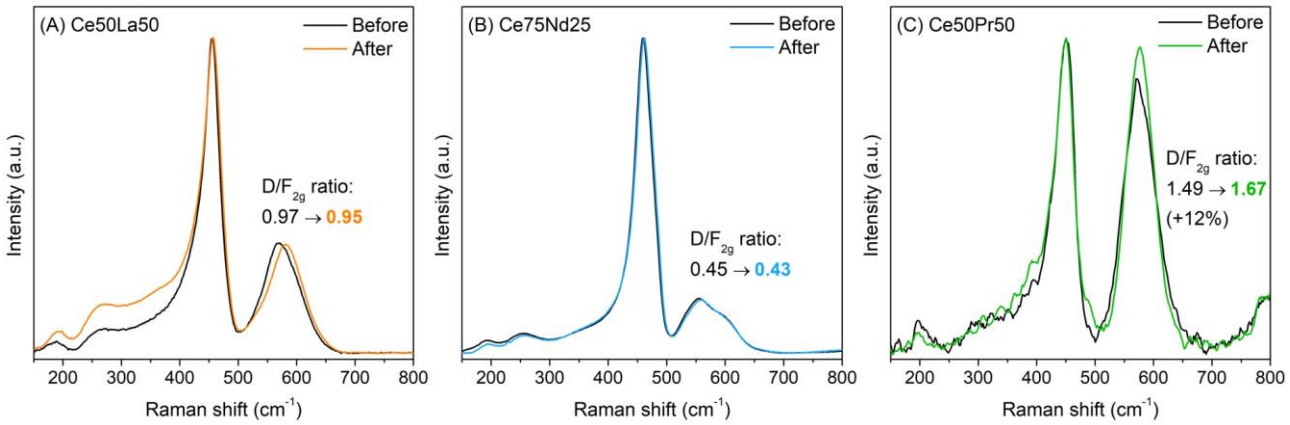

Fig. 15. Comparison of the Raman spectra collected at RT before (i.e. on fresh sample) and after soot oxidation for Ce50La50 (A), Ce75Nd25 (B) and Ce50Pr50 (C). The spectra are normalized to the F_{2g} peak intensity; the variation of the D/F_{2g} ratio is also reported.

Another remarkable difference between ceria-lanthana and ceria-praseodymia can be observed when carrying out soot oxidation in the presence of NO_x. In fact, as shown in Fig. 14 D, NO has a positive effect on soot oxidation both in loose and tight contact for Ce50Pr50, suggesting that alternative reaction pathways are promoted by this catalyst. Actually, a previous study has concluded that a heterogeneous mechanism occurs, involving not only NO to NO_2 oxidation but also NO_x adsorption and a direct participation of the superficial nitrates in the oxidation of soot particles [21]. This assumption is consistent with the presence of abundant basic sites with intermediate strength at the surface of the Ce50Pr50 sample, as can be noticed in Fig. 14 B and Table 7. Indeed, these medium sites allow the desorption of NO_x above 250 °C and their direct involvement in soot oxidation, as illustrated in Fig. 16. Instead, the excessive interaction between NO_x and the strong basic sites of Ce50La50 hinders this heterogeneous mechanism (Fig. 12 D).

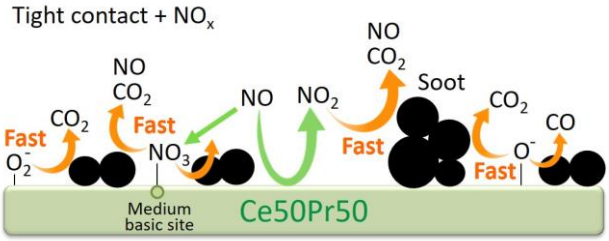

Fig. 16. Scheme reporting some of the possible reaction pathways occurring at the surface of the Ce50Pr50 catalyst during soot oxidation in tight contact in the presence of NO_x.

4. Conclusions

In this work, six ceria-based catalysts for soot oxidation were prepared by hydrothermal synthesis and carefully compared. La and Nd doping significantly affects the structural, physico-chemical and catalytic properties of ceria. These elements can be well-incorporated in ceria lattice, obtaining a fibrous morphology associated not only to a higher surface area but also to a better soot-catalyst contact. The Ce-O bonds are weakened in the mixed oxides, but this effect is counterbalanced by a lower quantity of available oxygen: in fact, a high La^{3+} or Nd^{3+} loading is associated with a huge increase of the catalyst defectiveness and of the concentration of oxygen vacancies, resulting in a less reducible oxygen-deficient material.

As a consequence, only moderate doping (10%) improves the CO oxidation activity, as a result of the weakened cerium-oxygen bonds. Instead, a further replacement of Ce with La or Nd leads to a progressive worsening of the catalytic performances, despite a greater surface area and defect abundance. This effect is due not only to the lower availability of active lattice oxygen in the highly doped samples, but also to the formation of stronger basic sites upon doping, which can hinder CO conversion. Analogously, the mixed oxides exhibit an activity for NO oxidation quite similar to that of pure CeO_2, without significant benefits from La and Nd addition. Conversely, soot oxidation is promoted by doping, especially in the case of the Ce75Nd25 and Ce50La50 samples.

In particular, the Ce-La equimolar mixture exhibited excellent catalytic properties, also outperforming analogous ceria-based oxides investigated in previous studies. This sample is indeed able to start soot combustion in loose contact below 400 °C in the presence of NO_x, despite its quite poor activity towards NO oxidation. Moreover, it seems very stable after thermal aging and can benefit from the presence of water in the gas stream.

Ceria-lanthana was then thoroughly compared with ceria-praseodymia, a better-known catalyst for soot oxidation, in order to clarify the origin of the outstanding performances of these two promising oxides. While Pr doping provides ceria with abundant redox sites and highly improved reducibility, the great intrinsic activity of Ce50La50 can be mainly ascribed to the large amount of active oxygen species and strong acid sites at its surface. In addition, different soot oxidation pathways are promoted by the two catalysts in the presence of NO_x: adsorbed nitrates are actively involved in the heterogeneous mechanism of Ce50Pr50, while they have a passive role in Ce50La50, replacing active oxygen species and thereby detrimentally affecting the activity in tight contact. The basic sites strength eventually determines the stability of the adsorbed NO_x, giving rise to the different behaviors.

In the end, equimolar ceria-lanthana is a really promising catalyst for soot oxidation and should be taken into account for future developments.

Declaration of interest

The authors declare no competing interests.

Acknowledgements

The authors greatly thank Gabriele Viglianco for helping in data collection during his MS thesis preparation. Camilla Galletti, Mauro Raimondo and Salvatore Guastella are kindly acknowledged as well for performing XRD, FESEM and XPS analyses.

Appendix A. Supplementary data

Supplementary material related to this article can be found, in the online version, at https://doi.org/10.1016/j.cattod.2021.11.040

References

[1] T. Johnson, A. Joshi, SAE Int. J. Engines. 11 (2018) 1307–1330.
[2] N. Hooftman, M. Messagie, J. Van Mierlo, T. Coosemans, Renew. Sustain. Energy Rev. 86 (2018) 1–21.
[3] S. Steiner, C. Bisig, A. Petri-Fink, B. Rothen-Rutishauser, Arch. Toxicol. 90 (2016) 1541–1553.

[4] F. Sapio, F. Millo, D. Fino, A. Monteverde, E. Sartoretti, A. Bianco, L. Postrioti, A. Tarabocchia, G. Buitoni, G. Brizi, SAE Tech. Pap. Ser. 1 (2019).
[5] B. Guan, R. Zhan, H. Lin, Z. Huang, J. Environ. Manage. 154 (2015) 225–258.
[6] D. Fino, S. Bensaid, M. Piumetti, N. Russo, Appl. Catal. A Gen. 509 (2016) 75–96.
[7] V. Di Sarli, A. Di Benedetto, AIChE J. 64 (2018) 1714–1722.
[8] E. Aneggi, C. de Leitenburg, M. Boaro, P. Fornasiero, A. Trovarelli, Catalytic applications of cerium dioxide, Elsevier Inc., 2020.
[9] V. Di Sarli, G. Landi, L. Lisi, A. Di Benedetto, AIChE J. 63 (2017) 3442–3449.
[10] M. Giuliano, M.C. Valsania, P. Ticali, E. Sartoretti, S. Morandi, S. Bensaid, G. Ricchiardi, M. Sgroi, Catal. 2021, Vol. 11, Page 247. 11 (2021) 247.
[11] M. Piumetti, S. Bensaid, T. Andana, M. Dosa, C. Novara, F. Giorgis, N. Russo, D. Fino, Catalysts. 7 (2017) 174.
[12] A. Trovarelli, J. Llorca, ACS Catal. 7 (2017) 4716–4735.
[13] Z. Wu, M. Li, S.H. Overbury, J. Catal. 285 (2012) 61–73.
[14] S. Agarwal, X. Zhu, E.J.M. Hensen, B.L. Mojet, L. Lefferts, J. Phys. Chem. C. 119 (2015) 12423–12433.
[15] M. Piumetti, B. van der Linden, M. Makkee, P. Miceli, D. Fino, N. Russo, S. Bensaid, Appl. Catal. B Environ. 199 (2016) 96–107.
[16] S. Bensaid, N. Russo, D. Fino, Catal. Today. 216 (2013) 57–63.
[17] H. Wang, B. Jin, H. Wang, N. Ma, W. Liu, D. Weng, X. Wu, S. Liu, Appl. Catal. B Environ. 237 (2018) 251–262.
[18] L. Soler, A. Casanovas, C. Escudero, V. Pérez-Dieste, E. Aneggi, A. Trovarelli, J. Llorca, ChemCatChem. 8 (2016) 2748–2751.
[19] I. Atribak, B. Azambre, A. Bueno López, A. García-García, Appl. Catal. B Environ. 92 (2009) 126–137.
[20] Q. Shen, G. Lu, C. Du, Y. Guo, Y. Wang, Y. Guo, X. Gong, Chem. Eng. J. 218 (2013) 164–172.
[21] T. Andana, M. Piumetti, S. Bensaid, N. Russo, D. Fino, Appl. Catal. A, Gen. 583 (2019) 117136.
[22] A. Bueno-López, Appl. Catal. B Environ. 146 (2014) 1–11.
[23] E. Sartoretti, C. Novara, F. Giorgis, M. Piumetti, S. Bensaid, N. Russo, D. Fino, Sci. Rep. 9 (2019) 3875.
[24] Y. Gao, A. Duan, S. Liu, X. Wu, W. Liu, M. Li, S. Chen, X. Wang, D. Weng, Appl. Catal. B Environ. 203 (2017) 116–126.
[25] D. Mukherjee, B.G. Rao, B.M. Reddy, Appl. Catal. B Environ. 197 (2016) 105–115.
[26] N. Guillén-Hurtado, A. García-García, A. Bueno-López, Appl. Catal. B Environ. 174–175 (2015) 60–66.
[27] T. Andana, M. Piumetti, S. Bensaid, L. Veyre, C. Thieuleux, N. Russo, D. Fino, E.A. Quadrelli, R. Pirone, Appl. Catal. B Environ. 226 (2018) 147–161.
[28] L. Katta, P. Sudarsanam, G. Thrimurthulu, B.M. Reddy, Appl. Catal. B Environ. 101 (2010) 101–108.
[29] A. Bueno-López, K. Krishna, M. Makkee, J.A. Moulijn, J. Catal. 230 (2005) 237–248.
[30] A.M. Hernández-Giménez, L.P.D.S. Xavier, A. Bueno-López, Appl. Catal. A Gen. 462–463 (2013) 100–106.
[31] S.S. Patil, H.P. Dasari, H. Dasari, Nano-Structures and Nano-Objects. 20 (2019) 100388.
[32] M. Dosa, M. Piumetti, S. Bensaid, T. Andana, C. Novara, F. Giorgis, D. Fino, N. Russo, Catal. Letters. 148 (2018) 298–311.
[33] R. Schmitt, A. Nenning, O. Kraynis, R. Korobko, A.I. Frenkel, I. Lubomirsky, S.M. Haile, J.L.M. Rupp, Chem. Soc. Rev. 49 (2020) 554–592.
[34] E. Aneggi, D. Wiater, C. De Leitenburg, J. Llorca, A. Trovarelli, ACS Catal. 4 (2014) 172–181.
[35] K. Kappis, J. Papavasiliou, ChemCatChem. 11 (2019) 4765–4776.
[36] E. Sartoretti, F. Martini, M. Piumetti, S. Bensaid, N. Russo, D. Fino, Catalysts. 10 (2020) 1–16.
[37] A. Umar, A.A. Ibrahim, R. Kumar, T. Almas, P. Sandal, M.S. Al-Assiri, M.H. Mahnashi, B.Z. AlFarhan, S. Baskoutas, Ceram. Int. 46 (2020) 5141–5148.
[38] Y. Li, J. Liu, D. He, Appl. Catal. A Gen. 564 (2018) 234–242.
[39] B. Huang, C. Huang, J. Chen, X. Sun, J. Alloys Compd. 712 (2017) 164–171.
[40] R. Lok, E. Budak, E. Yilmaz, J. Mater. Sci. Mater. Electron. 31 (2020) 3111–3118.
[41] S. Agarwal, L. Lefferts, B.L. Mojet, D.A.J.M. Ligthart, E.J.M. Hensen, D.R.G. Mitchell, W.J. Erasmus, B.G. Anderson, E.J. Olivier, J.H. Neethling, A.K. Datye, ChemSusChem. 6 (2013) 1898–1906.
[42] R.D. Shannon, Acta Crystallogr. Sect. A. 32 (1976) 751–767.
[43] S. Fernandez-garcia, L. Jiang, M. Tinoco, A.B. Hungria, J. Han, G. Blanco, J.J. Calvino, X. Chen, (2016).
[44] T. Andana, M. Piumetti, S. Bensaid, N. Russo, D. Fino, R. Pirone, Appl. Catal. B Environ. 197 (2016) 125–137.
[45] E. Sartoretti, C. Novara, M. Fontana, F. Giorgis, M. Piumetti, S. Bensaid, N. Russo, D. Fino, Appl. Catal. A Gen. 596 (2020) 117517.
[46] S. Agarwal, X. Zhu, E.J.M. Hensen, L. Lefferts, B.L. Mojet, J. Phys. Chem. C. 118 (2014) 4131–4142.
[47] C. Artini, M. Pani, M.M. Carnasciali, M.T. Buscaglia, J.R. Plaisier, G.A. Costa, Inorg. Chem. 54 (2015) 4126–4137.
[48] J. Cui, G.A. Hope, J. Spectrosc. 2015 (2015) 1–8.
[49] Z. Wu, M. Li, J. Howe, H.M. Meyer, S.H. Overbury, Langmuir. 26 (2010) 16595–16606.

[50] Y. Lee, G. He, A.J. Akey, R. Si, M. Flytzani-Stephanopoulos, I.P. Herman, J. Am. Chem. Soc. 133 (2011) 12952–12955.
[51] N. Paunović, Z. Dohčević-Mitrović, R. Scurtu, S. Aškrabić, M. Prekajski, B. Matović, Z. V. Popović, Nanoscale. 4 (2012) 5469.
[52] A. Filtschew, K. Hofmann, C. Hess, J. Phys. Chem. C. 120 (2016) 6694–6703.
[53] T. Vinodkumar, B.G. Rao, B.M. Reddy, Catal. Today. 253 (2015) 57–64.
[54] S.A. Acharya, V.M. Gaikwad, S.W. D'Souza, S.R. Barman, Solid State Ionics. 260 (2014) 21–29.
[55] C. Madhuri, K. Venkataramana, A. Nurhayati, C.V. Reddy, Curr. Appl. Phys. 18 (2018) 1134–1142.
[56] M. Lykaki, E. Pachatouridou, S.A.C. Carabineiro, E. Iliopoulou, C. Andriopoulou, N. Kallithrakas-Kontos, S. Boghosian, M. Konsolakis, Appl. Catal. B Environ. 230 (2018) 18–28.
[57] S.I. Boldish, W.B. White, Spectrochim. Acta Part A Mol. Spectrosc. 35 (1979) 1235–1242.
[58] A. Ubaldini, M.M. Carnasciali, J. Alloys Compd. 454 (2008) 374–378.
[59] Y. Wei, J. Liu, Z. Zhao, A. Duan, G. Jiang, C. Xu, J. Gao, H. He, X. Wang, Energy Environ. Sci. 4 (2011) 2959–2970.
[60] P. Yao, J. He, X. Jiang, Y. Jiao, J. Wang, Y. Chen, J. Energy Inst. 93 (2020) 774–783.
[61] T. Andana, M. Piumetti, S. Bensaid, N. Russo, D. Fino, R. Pirone, Nanoscale Res. Lett. 11 (2016) 1–9.
[62] M. Fingerle, S. Tengeler, W. Calvet, T. Mayer, W. Jaegermann, J. Electrochem. Soc. 165 (2018) H3148–H3153.
[63] S.D. Senanayake, D. Stacchiola, J. Evans, M. Estrella, L. Barrio, M. Pérez, J. Hrbek, J.A. Rodriguez, J. Catal. 271 (2010) 392–400.
[64] K. Polychronopoulou, A.F. Zedan, M. AlKetbi, S. Stephen, M. Ather, M.S. Katsiotis, J. Arvanitidis, D. Christofilos, A.F. Isakovic, S. AlHassan, J. Environ. Chem. Eng. 6 (2018) 266–280.
[65] C. Barth, C. Laffon, R. Olbrich, A. Ranguis, P. Parent, M. Reichling, Sci. Rep. 6 (2016) 2–7.
[66] T. Sakpal, L. Lefferts, J. Catal. 367 (2018) 171–180.
[67] Z. Li, K. Werner, K. Qian, R. You, A. Płucienik, A. Jia, L. Wu, L. Zhang, H. Pan, H. Kuhlenbeck, S. Shaikhutdinov, W. Huang, H.J. Freund, Angew. Chemie - Int. Ed. 58 (2019) 14686–14693.
[68] J. Lee, M.W. Lee, M.J. Kim, J.H. Lee, E.J. Lee, C.H. Jung, J.W. Choung, C.H. Kim, K.Y. Lee, J. Hazard. Mater. 414 (2021) 125523.
[69] M.F. Sunding, K. Hadidi, S. Diplas, O.M. Løvvik, T.E. Norby, A.E. Gunnæs, J. Electron Spectros. Relat. Phenomena. 184 (2011) 399–409.
[70] C. Yang, H. Fan, S. Qiu, Y. Xi, Y. Fu, J. Non. Cryst. Solids. 355 (2009) 33–37.
[71] M. Uma, N. Balaram, P.R. Sekhar Reddy, V. Janardhanam, V. Rajagopal Reddy, H.J. Yun, S.N. Lee, C.J. Choi, J. Electron. Mater. 48 (2019) 4217–4225.
[72] J.F. Moulder, W.F. Stickle, P.E. Sobol, K.D. Bomben, Handbook of X-ray Photoelectron Spectroscopy, Perkin-Elmer Corporation, Eden Prairie, Minnesota (USA), 1992.
[73] G. Gao, L. Yang, B. Dai, F. Xia, Z. Yang, S. Guo, P. Wang, F. Geng, J. Han, J. Zhu, Surf. Coatings Technol. 365 (2019) 164–172.
[74] E. Talik, M. Kruczek, H. Sakowska, Z. Ujma, M. Gała, M. Neumann, J. Alloys Compd. 377 (2004) 259–267.
[75] M. Ying, J. Hou, W. Xie, Y. Xu, S. Shen, H. Pan, M. Du, Sensors Actuators, B Chem. 260 (2018) 125–133.
[76] J. Jin, C. Li, C.W. Tsang, B. Xu, C. Liang, RSC Adv. 5 (2015) 102147–102156.
[77] F. Gaillard, 95 (2004) 23–29.
[78] C. Zhang, H. Huang, G. Li, L. Wang, L. Song, X. Li, Catal. Today. 327 (2019) 374–381.
[79] M. Piumetti, B. Bonelli, P. Massiani, S. Dzwigaj, I. Rossetti, S. Casale, L. Gaberova, M. Armandi, E. Garrone, Catal. Today. 176 (2011) 458–464.
[80] B. Azambre, L. Zenboury, J. V. Weber, P. Burg, Appl. Surf. Sci. 256 (2010) 4570–4581.
[81] Z. Wu, A.K.P. Mann, M. Li, S.H. Overbury, J. Phys. Chem. C. 119 (2015) 7340–7350.
[82] N. Hosseinpour, A.A. Khodadadi, Y. Mortazavi, A. Bazyari, Appl. Catal. A Gen. 353 (2009) 271–281.
[83] R.R. Nair, J. Arulraj, K.R. Sunaja Devi, Mater. Today Proc. 3 (2016) 1643–1649.
[84] P. Sudarsanam, B. Mallesham, P.S. Reddy, D. Großmann, W. Grünert, B.M. Reddy, Appl. Catal. B Environ. 144 (2014) 900–908.
[85] L. Katta, P. Sudarsanam, B. Mallesham, B.M. Reddy, Catal. Sci. Technol. 2 (2012) 995–1004.
[86] C. Binet, M. Daturi, J.C. Lavalley, Catal. Today. 50 (1999) 207–225.
[87] K. Kim, J. Do Yoo, S. Lee, M. Bae, J. Bae, W.C. Jung, J.W. Han, ACS Appl. Mater. Interfaces. 9 (2017) 15449–15458.
[88] V. Alcalde-Santiago, A. Davó-Quiñonero, D. Lozano-Castelló, A. Bueno-López, Appl. Catal. B Environ. 234 (2018) 187–197.
[89] P. Sudarsanam, B. Hillary, M.H. Amin, N. Rockstroh, U. Bentrup, A. Brückner, S.K. Bhargava, Langmuir. 34 (2018) 2663–2673.
[90] S. Liu, X. Wu, D. Weng, M. Li, R. Ran, ACS Catal. 5 (2015) 909–919.
[91] V. Di Sarli, G. Landi, L. Lisi, A. Saliva, A. Di Benedetto, Appl. Catal. B Environ. 197 (2016) 116–124.
[92] A.G. Konstandopoulos, M. Kostoglou, S. Lorentzou, N. Vlachos, Catal. Today. 188 (2012) 2–13.

[93] G. Kastrinaki, S. Lorentzou, A.G. Konstandopoulos, Emiss. Control Sci. Technol. 1 (2015) 247–253.
[94] W. Zhang, X. Niu, L. Chen, F. Yuan, Y. Zhu, Sci. Rep. 6 (2016) 1–10.
[95] J. Xu, G. Lu, Y. Guo, Y. Guo, X.Q. Gong, Appl. Catal. A Gen. 535 (2017) 1–8.
[96] C.S. Park, M.W. Lee, J.H. Lee, E.J. Jeong, S.H. Lee, J.W. Choung, C.H. Kim, H.C. Ham, K.Y. Lee, Mol. Catal. 474 (2019) 110416.
[97] Z. Shang, M. Sun, S. Chang, X. Che, X. Cao, L. Wang, Y. Guo, W. Zhan, Y. Guo, G. Lu, Appl. Catal. B Environ. 209 (2017) 33–44.
[98] E.E. Iojoiu, B. Bassou, N. Guilhaume, D. Farrusseng, A. Desmartin-Chomel, K. Lombaert, D. Bianchi, C. Mirodatos, Catal. Today. 137 (2008) 103–109.
[99] H. Zhang, S. Yuan, J.L. Wang, M.C. Gong, Y. Chen, Chem. Eng. J. 327 (2017) 1066–1076.
[100] Q.N. Tran, F. Martinovic, M. Ceretti, S. Esposito, B. Bonelli, W. Paulus, F. Di Renzo, F.A. Deorsola, S. Bensaid, R. Pirone, Appl. Catal. A Gen. 589 (2020).
[101] J.C. Martínez-Munuera, M. Zoccoli, J. Giménez-Mañogil, A. García-García, Appl. Catal. B Environ. 245 (2019) 706–720.
[102] S. Liu, X. Wu, W. Liu, W. Chen, R. Ran, M. Li, D. Weng, J. Catal. 337 (2016) 188–198.
[103] B. Azambre, S. Collura, P. Darcy, J.M. Trichard, P. Da Costa, A. García-García, A. Bueno-López, Fuel Process. Technol. 92 (2011) 363–371.
[104] A. Filtschew, C. Hess, Appl. Catal. B Environ. 237 (2018) 1066–1081.
[105] A. Westermann, C. Geantet, P. Vernoux, S. Loridant, J. Raman Spectrosc. 47 (2016) 1276–1279.
[106] S. Bensaid, M. Piumetti, C. Novara, F. Giorgis, A. Chiodoni, N. Russo, D. Fino, Nanoscale Res. Lett. 11 (2016) 1–14.